Università degli Studi di Cagliari

DOTTORATO DI RICERCA

FISICA

Ciclo XXVIII

TITOLO TESI

Degradation of Cd-yellow pigment: an ab initio study of defects and adsorption of oxygen and water on CdS

Settore/i scientifico disciplinari di afferenza

FIS 03 / Fisica della Materia

Presentata da:	*Laura Giacopetti*
Coordinatore Dottorato	*Prof. Alessandro De Falco* *Prof. Paolo Ruggerone*
Tutor	*Dott.ssa Alessandra Satta*

Esame finale anno accademico 2014 – 2015

University of Cagliari

DEPARTMENT OF PHYSICS
Ph.D. degree in Physics

Degradation of Cd-yellow pigment: an ab initio study of defects and adsorption of oxygen and water on CdS

Candidate:
Laura Giacopetti

Tutor:
Dott.ssa Alessandra Satta

Thesis submitted in 2015

Contents

List of Figures

List of Tables

Abstract

The cadmium yellow paints used in impressionist and modernist paintings in early 1900s are undergoing several deterioration processes, including whitening and discoloration. Relevant effects produced at the surface of modern paintings include the growth of discolored crusts, formed mainly by white globular hydrated cadmium sulfate $CdSO_4$*nH_2O and cadmium carbonate ($CdCO_3$). In view of the fact that the pigment, cadmium sulfide, was historically synthesized by means of dry and wet processes and that $CdCO_3$ and $CdSO_4$ are reagents for this procedure, their identification alone does not constitute conclusive proof of photo-oxidation. The origins of such chemical and physical alterations are still under debate.

Structural defects in CdS, among other possible causes like photo-oxidation processes, may play a role in the degradation process. Their presence in the pigment surface alters the electronic structure of cadmium sulfide by forming acceptor levels in the gap of the semiconductor. Such levels make the surface more reactive in the interaction with external agents (oxygen, water ...).

To this end, we present a theoretical study of points defects, namely Cd- and S- vacancies, in the structural wurtzite structure (bulk) and $[10\bar{1}0]$ CdS surface. In order to understand, at atomic level, the oxidation and hydration mechanisms of these whitish globules, we present the early stages of the interaction between the hexagonal clean and defective $[10\bar{1}0]$ surface of CdS and O_2 and H_2O molecules to simulate the combined effects of exposure to air and humidity.

The geometrical and electronic structures as well as the vacancy formation and adsorption energies are determined with the use of a first principles method. All the calculations are performed within the framework of the Density Functional Theory (DFT) in the Generalized Gradient Approximation (GGA-PBE) with the use of ultrasoft pseudopotentials. Despite the standard DFT-GGA ensures a correct order of electronic states, the G_0W_0 calculations are strongly required to attribute an accurate position of the trap level.

Considering the possibility to investigate in a broader spectral range, such theoretical method would be helpful in the interpretation of experimental evidences on fluorescence emissions produced from by yellow altered. This thesis highlights the key role that first-principles methods can play in the application of materials science to art conservation.

CHAPTER 1

Introduction

.... if you take some sand in your hand, if you look at it closely, and also water, and also air, they are all colorless, looked at in this way. There is no blue without yellow and without orange, and if you put in blue, then you must put in yellow, and orange too, mustn't you?

Vincent Van Gogh

1.1 Cadmium yellow

At present, cadmium sulfide (CdS) a member of II-VI wide-gap semiconducting compounds, is of considerable interest because of its potential applications in several science fields. Physical properties of CdS have been widely studied due to their importance in fundamental science as well as in optoelectronic applications like solar cells [4, 5, 6, 7], lasers [8, 9], and recently in nanotechnology [10, 11].

Given the importance in technology of these devices, the experimental and theoretical properties of such materials have drew much attention in recent years. Several theoretical methods have been successfully developed that allow the use of predictive *ab initio* simulations to investigate properties of materials [12, 13, 14]. Specially, by virtue of their high performance, semiconductors have been widely used as colour pigments in impressionist, post-impressionist and early modernist works from the 1880s through the 1920s. The strong yellow colouration of cadmium sulfide aroused great interest of artists soon after it was discovered. It was promptly added to the paint palette when the Impressionists were experimenting with colour, and is now a reliable standard of the paint box. His first appearance, in artistic field, has been onto canvasses in the 1840's in the work of that great artist of yellow, Vincent van Gogh (though his famous sunflowers primarily used chrome yellow), followed by prominent 19th to 20th century artists such as Claude Monet, Pablo Picasso and Henry Matisse. Cadmium sulfide occurs in nature with two different crystal structures: the rare minerals greenockite and hawleyite. The more stable hexagonal wurtzite structure was found in the mineral Greenockite and the cubic zinc blende structure was found in the mineral Hawleyite. The amorphous form is only known as a chemically synthesized product [15].

The brilliant yellow pigment, takes all its colouration from cadmium sulfide -which is observed in many pigments in the hexagonal wurtzite phase [16, 17]- that is confirmed to be the main crystalline constituent of the yelllow paint. It was produced in 1817 by the German Stromeyer, but its use as an artists's pigment began about one year later. Cadmium reds remained in limited use until around the 1920s [18]. Cadmium with golden-yellow colour and high chroma forms the basis for all cadmium pigments. The chromatic variation of these pigments depends on their chemical composition, crystalline structure, and on their history in the synthesis process. The pigment cadmium sulfide was historically produced by means of either a dry or a wet process, as stated by Fiedler and Bayard [18]. For the dry process, either metallic cadmium, cadmium oxide, or cadmium carbonate was employed as starting material.

During the wet process, CdS was obtained as a precipitate by adding a soluble sulfide (such as hydrogen sulfide, sodium sulfide, or barium sulfide) to a soluble cadmium salt (such as cadmium chloride, cadmium nitrate, cadmium sulfate, or cadmium iodide) [19].

However, in spite of its excellent reputation with regards to permanency, the degradation of cadmium yellow occurs primarily in the lighter yellows, and involves discolouration (fading and darkening) producing chalking and crumbly surfaces. This alteration was ascribed to an initial photo-oxidation of CdS: excitation of material by visible light (absorption of photons with energy equal to the band gap) and formation of electron/hole pairs [20]. Subsequently, the cadmium compound itself decays as the positive holes (h^+) oxidize the solid [21].

After further oxidation, by atmospheric oxygen, of the sulfur S^0 that becomes SO_4^{2-}. The overall reaction becomes

$$CdS + 2O_2 \longrightarrow Cd^{2+} + SO_4^{2-} \tag{1.1}$$

The soluble cadmium sulfate is thus supposed to re-precipitate in the form of white globules on the yellow paint layer.

The presence of whitish semitransparent globules ($CdSO_4$*nH_2O) and cadmium carbonate ($CdCO_3$) have been identified [22, 23, 24] in degraded areas and considered such as photo-oxidation products.

In general, elucidating origins and roles of this compounds is an arduous task. In fact, in the synthesis of cadmium sulfide, for instance, reagents such as $CdCO_3$ and $CdSO_4$ were employed both in the dry and wet processes as paint fillers or starting reagents. Their identification alone does not conclusively make them sub-products of photo-oxidation processes because traces of them are also found within layers away from the surface, to confirm their employ such as starting reagents.

1.1.1 Previous experimental studies

For a long time, the complex alteration of cadmium sulfide was studied [25, 22, 23, 24, 26, 27, 28]. Indeed, this compound was known to suffer from degradation under the influence of sunlight and humidity. Despite the fact this phenomenon is rather ambiguous and does not take place systematically, recent hypothesis have been given to explain the discolouration process. A gradual fading of originally bright yellow areas, painted with the pigment cadmium yellow paints, is observed in the following works: *Still Life with Cabbage* [22] by James Ensor, *The Joy of Life* [23, 24] and *Flower Piece* [26] by Henri Matisse.

The first study on CdS pigment alteration was performed in 2005 by Leone *et al.* [27] on 12 samples of cadmium pigments dating from 1887-1923. In this study the presence of $CdSO_4$, $CdCO_3$, $Cd(OH_2)$ in the surface of painting suggested a preliminary degradation mechanism due to high relative humidity conditions that increase the loss of degrading cadmium yellow paint film's structural integrity.

Van der Snickt et al [22] in the Ensor painting *Still Life with Cabbage*, found local variation in color intensity after removal of the frame of the painting, where the cadmium yellow seemed to have largely preserved its original color respect to the rest of the painting. This suggested that the observed alteration was induced by environmental causes. In particular, repeated hydration and drying of the paint surface resulted in the formation of semi-transparent whitish globules of $CdSO_4$*nH_2O. In the degraded areas containing ($CdSO_4$*nH_2O), ultraviolet illumination yielded an orange fluorescence, whereas the non-degraded paint gave forth a brown fluorescence. The origin of these fluorescent emissions has not been conclusively established and further analyses with better resolution are necessary in non-degraded yellow areas of the painting.

As suggested from these studies [23, 24, 26], a substantial enrichment of $CdCO_3$ and

$CdSO_4$*nH_2O in the off-white surface occurred in *The Joy of Life* by Matisse. The analysis of altered samples removed from painting confirm the $CdCO_3$ near the surface to be present as an insoluble photodegradation product of a gradual secondary reaction of $CdSO_4$ with atmospheric CO_2. Its high concentration in the yellow interior of the paint layer, however, is open to two interpretations: it may suggest an advanced progression of the photo-oxidation and also demonstrate that the original cadmium yellow paint formulation contained a $CdCO_3$ filler. [28]. The cadmium ($CdSO_4$*nH_2O) could be present as a leftover synthesis reagent, or as a photo-oxidation product although it is not yet visible as a color change. Furthermore, the high solubility of $CdSO_4$*nH_2O could also explain its distribution throughout the paint layer complicating even more the interpretation.

High concentration of $CdCO_3$ have been also observed in another painting, Edvard Munch's *The Scream*, and interpreted as being from an indirect wet process starting material and/or a $CdCO_3$ filler rather than being conclusive evidence for photo-oxidation [28]. Another case of CdS alteration but with different macroscopic effect, is in the painting *Flowers in a blue vase* by Vincent van Gogh. Van der Snickt et al [17] found the opaque crust in several CdS paint areas. The observed degradation was initially caused by oxidation of the original CdS pigment in Cd^{2+} and SO_4^{2-} as previously found on Ensor's *Still Life with Cabbage* [22]. This ions could have then reacted with $C_2O_4^{2-}$ and Pb^{2+} from unoriginal varnish, likely applied after the initial deterioration of the CdS yellow.

In order to complete the interpretation of degradation materials, Pouyet *et al.* [26], using analytical methods with a high sensitivity and ability to map the distribution of CdS proposed an explanation of the synthesis and degradation pathways of cadmium pigments in several paintings. Distribution of various cadmium compounds in altered paints confirms that cadmium carbonates and sulphates are photo-degradation products in *The Joy of Life*, whereas in *Flower Piece*, a large amount of cadmium carbonate present in unchanged yellow may be related to a partially unreacted starting reagent. Indeed, it is not accumulated at the paint surface but co-located in a core of individual CdS yellow pigment particles visible thanks to their orange fluorescence in the ultraviolet.

Luminescence spectroscopy has been employed in the field of cultural heritage for many years [29, 30, 31] to identify forgeries in oil paintings, varnish heterogeneous restoration, and in some cases to identify and map multiple pigments in situ in the same work of art.

Several pigments used in oil colors are composed of semiconductors and organic dyes that show different spectra and decay characteristics of fluorescence [32, 33]. In the specific case of CdS, in addition to the band edge emission in the visible range, cadmium pigments show an emission in the red to near-infrared associated to trap states within the band gap, likely due to impurities and/or crystal defects [34].

Also, early publications [31, 35, 36] on the luminescence properties of cadmium pigments reported emissions in the red to near-infrared plausibly related to trap emissions. Anyhow, in most cases the exact origin of these emissions could not be explicitly stated.

In order to better understand the origin of their color and luminescence in the paint layers recent studies [37, 38, 39, 40, 41] focused on luminescence emission lifetimes of luminescent materials. Cd- and Zn-based pigments, were characterized [40] both by a rapid picosecond lifetime band gap emission related to pigment composition and by further radiative relaxation decay paths due to trap state levels connected to the presence of intrinsic and extrinsic defects. The first application of lifetime imaging [41] for the mapping of long-lived luminescence from the ZnO semiconductor pigment was on the painting on paper "Les bretonnes et le pardon de pont Aven" by Vincent Van Gogh. In this work it was demonstrated how metal impurities in the crystal lattice give rise to the formation of electron-hole recombination centers, by inducing the formation of extra energy levels.

Results obtained in bulk CdS have shown two red-near infrared emission bands associated to deep trap states in the band gap , namely E_{t1} and E_{t2}, with values of wavelengths in the ranges 640-710 nm for E_{t1} and 680-900 nm for E_{t2}. The role of impurities in the crystal lattice introduced during pigment synthesis as well as surface dangling bonds is invoked as responsible in the formation of these trap states.

Moreover, measurements and models on nanoparticles of CdS were conducted to understand optical properties of these nanostructured materials. Varghese *et al.* [42], by means of a combination of experiments and ab initio calculations based on density functional theory, studied the absorption and photoluminescence properties of CdS nanotubes related to Cd and S vacancies. The results of this work suggest that rather than the concentration, it is the nature of the defect crucial in photoluminescence spectra.

Also, semiconducting compounds related to red bright pigments HgS favoured by Rubens and italian masters, revealed features very similar to CdS. Hogan *et al.* [43, 44] by means of a first-principles study based on state-of-the-art electronic structure methods and high-resolution microscopic x-ray diffraction clarify the mechanism of undesirable phenomenon of degradation where the bright red pigment vermilion (α-HgS) turns into black colour.

It is known [45] that the presence of defects breaking the translational symmetry of the crystal lattice induces changes both in the geometry of the crystal itself and in the electronic structure. The atoms neighboring the defects, in fact, displace from equilibrium positions and such displacements correspond to a rearrangement of the electron states in the valence energy region close to the Fermi level and, especially in semiconductors, within the gap itself.

The most common defects include point defects and impurities. The first ones, native point defects, are single- and/or di-vacancies. They consist in single cation/anion vacant sites or couples of them. An impurity is a chemical element, different from native cations and anions, occupying substitutional positions or interstitial sites in the pristine crystal lattice. The presence, the concentration and the behaviour of any of these defects in a crystalline structure depends mostly on the history of the sample: growing or synthesis techniques, environment conditions during the growth, environment conditions after the growth. Every single one of them is differently detectable and shows itself with specific features. Vacancies and impurities in semiconductors, for instance, are likely to create new empty or occupied energy levels acting as acceptor or donor levels within the gap [46]. This fact modifies the original gap and changes the behaviour and the reactivity of the semiconductor, accordingly. In any case, they are trap states for excited electrons and their precise location in the electronic structure gives a relevant amount of information on the sample under investigation.

1.2 Scope of this Thesis

Both historic mineral-based pigments and modern synthetic pigments used in painting are susceptible to alteration as a result of their reactions with light, atmospheric moisture, oxygen and other agents of degradation present in the environment. The degradation mechanisms behind these alterations are often complex, involving traces of synthesis starting reagents or other impurities in the paint, requiring the presence of multiple degradation agents.

In this work the aforementioned degradation process in yellow-cadmium pigments is linked to the presence of structural defects in CdS crystal lattice. In particular, we focus on the role of Cd- and S- vacancies in the most stable CdS surface, namely the $[10\bar{1}0]$, and their interaction with oxygen and water.

In the first part of thesis we focus the attention on the role of Cd- and S- vacancies in the bulk in wurtzite phase and in the $[10\bar{1}0]$ surface. In the second part, elementary reactions between the surface and oxygen/water molecules are given in the attempt to contribute preliminarily to the debate on the photo-oxidation mechanisms experimentally invoked to interpret the appearance of the whitish globules in the paint surface. To this end the $[10\bar{1}0]$ surface of CdS was considered with and without defects, as a benchmark. It was simulated according to the slab geometry and was next covered by oxygen, water molecules and a combination of O_2 + H_2O. More specifically, we determined the favorite adsorption sites and calculated the adsorption energies of the different molecules on top of the surface. The details of the electronic structure at the interface are given via density of states and bonding charge analysis along with a thorough description of the geometry.

All the calculations are performed within the framework of the Density Functional Theory (DFT) in the Generalized Gradient Approximation (GGA-PBE) with the use of ultrasoft pseudopotentials.

GW approximation allowed us to accurately estimate the band gap of bulk CdS that combined with the Kohn and Sham bang gap center lead to a good approximation of the band edges and an estimate of extra energy levels in the gap of defective structures. A precise location of trap states still requires approaches able to fully deal with excited states but yet, the overall picture obtained at this level of theory allows to add reliable information to the debate on photoluminescence issues about the process of alteration of cadmium yellow.

In other words, such theoretical approach allows to: *i)* tackle separately the effects of every kind of defects giving an accurate description of the geometry, the energetics and the electronic structure of the systems containing them; *ii)* link the type of defects to experimental evidences - often obtained from heterogeneous samples - with the aim of contributing to untangle the superposition of effects originating from different physical-chemical events. *iii)* simulate the combined effects of exposure to air and humidity by means of the interaction between the clean and defective $[10\bar{1}0]$ surface of CdS and O_2 and H_2O molecules.

Theoretical modelling plays an important role in the field of conservation of works of art. With powerful predicting features, it is complementary to the experimental investigation and is of great support in the interpretation of results.

CHAPTER 2

Theoretical Background

In this Chapter the crucial ingredients of the density functional theory (DFT) are presented along with a description of different exchange and correlation functionals and pseudopotentials. The GW approximation, adopted to correct the underestimated band gap in bulk CdS, is also briefly illustrated.

2.1 Electronic structure problem

To understand the electronic structure of defects in semiconductors and the properties of interacting defects within the bulk, it is natural to consider the solution to the Schrödinger equation for a system of N interacting particles with M ions, expressed in the time independent form as

$$\hat{H}\Psi(\{\mathbf{R_A}\},\{\mathbf{r_i},\sigma_{\mathbf{i}}\}) = E\Psi(\{\mathbf{R_A}\},\{\mathbf{r_i},\sigma_{\mathbf{i}}\}) \tag{2.1}$$

Where E represents the total energy of the system and Ψ is the many-body wavefunction or (eigenfunction) for the N electronic eigenstates, an anti-symmetric function of the electronic coordinates ($\{\mathbf{r_i},\sigma_i\}$, i = 1,..., N) and spatial coordinates of nuclei ($\{\mathbf{R_A}\}$, A = 1, ..., M). The Hamiltonian operator ($\hat{H}$) is a sum of all possible interactions between electrons and nuclei. In atomic units (energy in Hartree and length in Bohr) is represented by:

$$\hat{H} = -\sum_{i=1}^{N}\frac{\nabla_i^2}{2} - \sum_{A=1}^{M}\frac{\nabla_A^2}{2M_A} + \sum_{i=1}^{N}\sum_{j>i}^{N}\frac{1}{|r_i - r_j|} + \sum_{A=1}^{M}\sum_{B>A}^{M}\frac{Z_A Z_B}{|R_A - R_B|} - \sum_{i=1}^{N}\sum_{A=1}^{M}\frac{Z_A}{|r_i - R_A|} \tag{2.2}$$

Here, M_A is the ratio of the mass of nucleus A to the mass of an electron and Z_A is the atomic number of nucleus A. The ∇_i^2 and ∇_A^2 are the Laplacian operators. These five summation terms in above equation represent the kinetic energies of all the electrons and nuclei, the Coulomb repulsion between electrons and between nuclei and the Coulomb attraction between electrons and nuclei. The Schrödinger equation has the appearance of being rather simple by its form but is enormously complex to solve, because the electron-electron interaction term, which contains all the many-body physics of the electronic structure problem and depends at least on $3N$ spatial coordinates. The Born-Oppenheimer approximation [47] is the first important assumption to reduce the complexity of the system. This approximation is obtained by decoupling the dynamics of the electrons and the nuclei.

2.1.1 Born-OppenheimerApproximation

In this section, we will discuss one of the most important and fundamental approximations developed by Max Born and J. Robert Oppenheimer in 1927 [47]. The fundamental aim of the Born-Oppenheimer approximation comes from the fact that because the nuclei are much heavier than the electrons, their kinetic energy (motion) can be neglected. Since the nuclei are considerably more massive than the electrons, in most cases the timescale of the response of the electrons is a few orders of magnitude faster than that of the nuclei. This allows that, the dynamics of the electrons and nuclei to be decoupled. Under this simple approximation, nuclei can be considered as classical particles and can be assumed as static with respect to quantum particle electrons. Then for any given nuclear configurations the electrons are considered to remain in their instantaneous ground state. Consequently, the second term in Eq. (2.2) vanishes and the fourth term, the repulsion between nuclei, becomes a constant for a fixed configuration of the nuclei. The remaining terms in Eq. (2.2) are called the electronic Hamiltonian ($\hat{H}_e$), in which the position of the nuclei are only parameters, leading to,

$$\hat{H}_e = -\sum_{i=1}^{N}\frac{\nabla_i^2}{2} + \sum_{i=1}^{N}\sum_{j>i}^{N}\frac{1}{|\mathbf{r_i} - \mathbf{r_j}|} - \sum_{i=1}^{N}\sum_{A=1}^{M}\frac{Z_A}{|\mathbf{r_i} - \mathbf{R_A}|} \tag{2.3}$$

As a result, the Schrödinger equation involving the electronic Hamiltonian ($\hat{H}_e$) becomes:

$$\hat{H}_e \Psi_e(\{\mathbf{R_A}\}, \{\mathbf{r_i}, \sigma_\mathbf{i}\}) = E_e \Psi_e(\{\mathbf{R_A}\}, \{\mathbf{r_i}, \sigma_\mathbf{i}\}) \tag{2.4}$$

The electronic wavefunction (Ψ_e) of the new obtained Schrödinger equation, depends on nuclear coordinates ($\{\mathbf{R_A}\}$) only parametrically. Moreover, for convenience, we can repress ($\{\mathbf{R_A}\}$) for fixed configuration of nuclei and assemble electronic spatial and spin coordinates ($\{\mathbf{r_i},\sigma_i\}$) in to one variable ($\{\mathbf{x_i}\}$ (i.e., $\{\mathbf{x_i}\} = \{\mathbf{r_i},\sigma_i\}$) and rewrite Eq. (2.4) as

$$\hat{H}_e \Psi_e(x_i) = E_e \Psi_e(x_i) \tag{2.5}$$

For some fixed configurations of the nuclei, the total energy will also include the constant nuclear repulsion term expressed as

$$E_{tot} = E_e + \sum_{A=1}^{M} \sum_{B>A}^{M} \frac{Z_A Z_B}{|\mathbf{R_A} - \mathbf{R_B}|} \tag{2.6}$$

Total energies are obtained , under the Born-Oppenheimer approximation, to solving equations resembling (2.5) and (2.6) in this way reducing the electronic structure problem. For most condensed matter systems, the Born-Oppenheimer approximation is highly accurate but is certainly not universally valid. The interaction between electrons, where all the many-body quantum effects are hidden, is the major difficulty in solving Eq. (2.5). The Treatment of 3^N variables for an N-electron system is essentially required, when we consider the motion of the electrons and the instantaneous coordinates of each electron. Approximate methods have been necessary to solve Schrödinger or Schrödinger-like equations by mapping the N-electron Schrödinger equation in to effective one-electron Schrödinger-like equations. These approximate solutions may be divided into in to two major branches: *i)* wave function theory (WFT) approaches, where one uses variational methods, perturbation theory, or many-body theory to achieve an approximate solution of the Schrödinger equation, *ii)* density functional theory (DFT) which provides the ground state properties of a system and where the electron density plays a key role [48, 49]. Here, the DFT based methods will be introduced in details.

2.2 Density functional theory

Density-functional theory is presently one of the most popular and successful computational quantum mechanical modelling approaches to matter, because it was shown provide a advantageous balance between accuracy and computational cost. At present, DFT is the mainstay of electronic structure calculations in solid-state physics and was widely applied for calculating, e.g., on superconductivity, magnetic properties of alloys, atoms in the focus of strong laser pulses, relativistic effects in heavy elements and in atomic nuclei. Moreover, in conservation of cultural heritage, the theoretical calculations can be applied to the understanding the mechanisms which induce the degradation, to clarify the composition of the damaged paint work [43, 44] and in our specific case the role of defects in crystal lattice of altered semiconductor pigment. The primary purpose of DFT is to reduce the $3N$ variable Schrödinger equation to a three variable function of the electron density $\rho(\mathbf{r})$. This reduction was proved by two theorems of Pierre Hohenberg and Walter Kohn [50]. The use of electron density as a fundamental description of the system is more attractive because considers only of three variables x, y, z, and eventually, if you count in spin, the densities for spin polarized systems, one for spin up electrons $\rho_{\uparrow}(\mathbf{r})$ and one for spin down electrons $\rho_{\downarrow}(\mathbf{r})$. In particular, according to the second theorem proved by them, the total ground state energy of an electron system can be written as a functional of the electronic density, and this energy is at minimum if the density is an exact density for the groud state. The modern formulation of modern Density Functional Theory (DFT) was proved by Hohenberg and Kohn in 1964 with the publication of the Hohenberg and Kohn paper [50]. This formally is based on two ingeniously simple theorems:

I. For any system of N interacting electrons in a non-degenerate ground state associated with an external potential $\hat{V}_{ext}$, the ground state electron density determines this potential uniquely. The external potential is a unique functional of the ground state electron density

II. The ground state density can be found, in principle exactly, by employing the variational method considering only density (to within an additive constant)

These theorems were derived by quite an original logic, that establish the connection between the electron density and the many-electron Schrödinger equation. Within the Born-Oppenheimer approximation, the ground state of the system of electrons is a result of positions of nuclei, as shown in electronic Hamiltonian ($\hat{H}_e$) equation:

$$\hat{H}_e = \hat{T}_e + \hat{V}_{ext} + \hat{U}_{ee} \tag{2.7}$$

The results of this hamiltonian, the kinetic energy of electrons ($\hat{T}_e$) and the electron-electron interaction ($\hat{U}_{ee}$) arising from the nuclei is treated as a static external potential potential $\hat{V}_{ext}$. In the electronic Hamiltonian, the external potential $\hat{V}_{ext}$ is the only variable and everything else depends indirectly on it. Since $\rho(\mathbf{r})$ determines the probability of finding any of the number of electrons, N within the volume $\mathbf{r}$:

$$N = \int \rho(\mathbf{r}) d\mathbf{r} \tag{2.8}$$

If the first theorem is proven $\rho(\mathbf{r})$ determines the $\hat{V}_{ext}$, and the whole electronic Hamiltonian can be expressed as a functional of $\rho(\mathbf{r})$. They proved it through a contradiction, using the principle of reductio ad absurdum, and this is derived for a non-degenerate system.

Assume that we have an exact ground state density $\rho(\mathbf{r})$ and is valid for a non-degenerate ground state (i.e., there is only one wave function Ψ for this ground state and by means HK theorems can be easily extended for degenerate ground states, see, e.g., Dreizler & Gross [51]; Kohn [52]). Suppose that for the density $\rho(\mathbf{r})$ there are two possible external potentials: $\hat{V}_{ext}$ and $\hat{V}'_{ext}$, which have two different hamiltonians $\hat{H}_e$ and $\hat{H}'_e$, and conseguently two different ground state: Ψ and Ψ', for the ground state density. They correspond to ground state energies: $E_0 = \langle \Psi | H | \Psi \rangle$ and $E'_0 = \langle \Psi' | H' | \Psi' \rangle$, respectively. Then, using variational theorem, we will have the expectation value of energy for the Ψ' with the hamiltonian $\hat{H}$:

$$E_0 < \langle \Psi' | H | \Psi' \rangle = \overbrace{\langle \Psi' | H' | \Psi' \rangle}^{E'_0} + \langle \Psi' | H - H' | \Psi' \rangle = E'_0 + \int \rho(\mathbf{r}) [\hat{V}_{ext} - \hat{V}'_{ext}] d\mathbf{r} \tag{2.9}$$

Then, using variational theorem, we will have expectation value of energy for the Ψ with the hamiltonian $\hat{H}'$:

$$E'_0 < \langle \Psi | H' | \Psi \rangle = \underbrace{\langle \Psi | H | \Psi \rangle}_{E_0} + \langle \Psi | H' - H | \Psi \rangle = E_0 - \int \rho(\mathbf{r}) [\hat{V}_{ext} - \hat{V}'_{ext}] d\mathbf{r} \tag{2.10}$$

Adding equations (2.9) and (2.10) we get:

$$E_0 + E'_0 < E'_0 + E_0 \tag{2.11}$$

which is an obvious contradiction. Therefore, the external potential is a unique functional of the ground state electron density.

Thus, we know that $\rho(\mathbf{r})$ determines N-elettrons, $\hat{V}_{ext}$ and also all properties of the ground state. We can write the total ground state energy as a functional of density with the following components:

$$E_v[\rho] = T_e[\rho] + V_{ext}[\rho] + U_{ee}[\rho] = \int \rho(\mathbf{r}) \hat{V}_{ext}(\mathbf{r}) d\mathbf{r} + F_{HK}[\rho] \tag{2.12}$$

where

$$F_{HK}[\rho] = T_e[\rho] + U_{ee}[\rho] \tag{2.13}$$

The F_{HK} is a universal functional of $\rho(\mathbf{r})$, its form does not depend from any external potential, includes all internal energies, kinetic and potential, of the interacting electron system. The second HK theorem provides variational principle in electron density representation $\rho(\mathbf{r})$ that minimizes the total energy being the exact ground state density. This is expressed as:

$$E_v[\rho] \geq E_0[\rho_0] \tag{2.14}$$

where ρ_0 is the exact density and E_0 is the ground-state energy for N electrons in the given external potential. Suppose the ground state wave function is Ψ and its related electron density is $\rho(\mathbf{r})$. Thus the electron density uniquely determines the external potential V_{ext}. If we consider another trial wave function Ψ' and its electron density is $\rho'(\mathbf{r})$, then we can obtain

$$\langle \Psi' | H | \Psi' \rangle = \int \rho'(\mathbf{r}) \hat{V}_{ext}(\mathbf{r}) d\mathbf{r} + F_{HK}[\rho'] = E[\rho'] \geq E[\rho] \tag{2.15}$$

by the variational principle. In other words, if some density represents the correct number of electrons N, the total energy calculated from this density cannot be lower than the true energy of the ground state [53].

It follows that if the functional F_{HK} was known, the solution would be a straightforward minimization of the energy functional, with respect to variations in the density function $\rho(\mathbf{r})$ in three-dimensional space. However, the problem, is that the exact form of F_{HK} is unknown and the major part of the complexities of the many-electron problem can not be solved with the determination of the universal functional. To address this problem, Kohn and Sham propose a solution to this problem by introducing an approximation for the unknown functional F_{HK} [48, 54].

2.2.1 The Kohn-Sham Equations

To employ the DFT formalism one obviously needs an accurate approximation for the functional F_{HK}, that have been obtained by means of the Kohn-Sham method [55]. They recognized that, the original Thomas-Fermi theory is quite unsatisfactory for atoms and molecules, in particular relating to description of kinetic energy. For that reason, Kohn & Sham proposed an useful method (similar to the Hartree-Fock approach) where they re-introduced the idea of non-interacting electrons moving in an effective field. We can now rewrite the energy functional obtained in the previous

Eq. (2.12) into following parts:

$$E[\rho] = \int \rho(\mathbf{r})\hat{V}_{ext}(\mathbf{r})d\mathbf{r} + F_{HK}[\rho] = \int \rho(\mathbf{r})\hat{V}_{ext}(\mathbf{r})d\mathbf{r} + T_0[\rho] + E^{Hartree}[\rho] + E_{xc}[\rho] \tag{2.16}$$

where F_{HK} is written as a sum of the kinetic energy of electrons (T_0) in a system which has the same density ρ as the real system (no electron-electron interactions), the Hartree energy ($E^{Hartree}$), and the exchange and correlation energy (E_{xc}). The latter functional includes all the energy contributions which were not accounted for by previous terms, i.e. (electron exchange, electron correlation, since non-interacting electrons do need to correlate their movements, a portion of the kinetic energy which is needed to correct $T_0[\rho]$ to obtain true kinetic energy of a real system $T_e[\rho]$, correction for self-interaction introduced by the classical coulomb potential).

In the next step we can define an effective potential depending upon $\mathbf{r}$:

$$\hat{V}_{eff}(\mathbf{r}) = \hat{V}_{ext}(\mathbf{r}) + \hat{V}_H(\mathbf{r}) + \hat{V}_{xc}(\mathbf{r}) \tag{2.17}$$

In the above equation the $\hat{V}_H(\mathbf{r})$ is Hartree potential, while the exchange correlation potential is defined as a functional derivative of exchange correlation energy:

$$\hat{V}_{xc}(\mathbf{r}) = \frac{\delta E_{xc}[\rho(\mathbf{r})]}{\delta\rho(\mathbf{r})} \tag{2.18}$$

Now, in order to find the ground state density and energy we need to solve the Schrödinger equation for noninteracting particles like Kohn-Sham equations:

$$\left[-\frac{1}{2}\nabla_i^2 + \hat{V}_{eff}(\mathbf{r})\right]\phi_i^{KS}(\mathbf{r}) = \epsilon_i\phi_i(\mathbf{r})^{KS} \tag{2.19}$$

This equations are analogous to the equation of the Hartree-Fock[1] method, but these result simpler. Indeed, the Kohn-Sham operator depends only on $\mathbf{r}$, and not upon the index of the electron, resulting similar for all electrons. The Kohn-Sham orbitals, $\phi_i(\mathbf{r})^{KS}$ are easy enough obtained from this equation and the total density is given by

$$\rho(\mathbf{r}) = \sum_{i=1}^{N} |\phi_i^{KS}(\mathbf{r})|^2 \tag{2.20}$$

which can be used to calculate an improved potential $\hat{V}_{eff}(\mathbf{r})$. So the Kohn-Sham equation must be solved self-consistently. The self-consistent procedure involves the

---

[1] Fock operator is defined as: $\hat{f}(\mathbf{r_1})\phi_\mathbf{i}(\mathbf{r_1}) = \epsilon\phi_\mathbf{i}(\mathbf{r_1})$ and contains the potential which is nonlocal, i.e., different for each electron.

following steps: *i)* start with an initial guess for the density; *ii)* construct $\hat{V}_{eff}(\mathbf{r})$, and solve the Kohn-Sham Eq. (2.19); *iii)* then get the Kohn-Sham orbitals to update the density obtained from Eq. (2.20). This process repeated until convergence is achieved i.e., until the Kohn-Sham equations return the input density. Density can also be used to calculate the total energy from Eq. (2.16), in which the kinetic energy $T_0[\rho]$ is calculated from the corresponding orbitals, rather than density itself:

$$T_0[\rho] = \frac{1}{2}\sum_{i=1}^{N} \langle \phi_i^{KS} | \nabla_i^2 | \phi_i^{KS} \rangle \tag{2.21}$$

and the rest of the total energy as:

$$V_{eff}[\rho] = \int \hat{V}_{eff}(\mathbf{r})\rho(\mathbf{r})d\mathbf{r} \tag{2.22}$$

Now, total energy is calculated more easily using energies of the Kohn-Sham one-electron orbitals ϵ_i as:

$$E[\rho] = \sum_{i=1}^{N} \epsilon_i - \frac{1}{2}\int\int \frac{\rho(\mathbf{r})\rho(\mathbf{r}')}{|\mathbf{r}-\mathbf{r}'|} d\mathbf{r}d\mathbf{r}' - \int \hat{V}_{xc}(\mathbf{r})\rho(\mathbf{r})d\mathbf{r} + E_{xc}[\rho] \tag{2.23}$$

In conclusion, we can calculate the total energy from Eq. (2.23), obtained from famous Kohn-Sham equations (2.16, 2.19, 2.20), with the final electron density. If we know each term in the Kohn-Sham energy functional, we would be able to obtain the exact ground state density and total energy. Unfortunately, the simplicity and formal exactness of the Kohn-Sham theory come with a price. The exact exchange-correlation functional is unknown and must be approximated for any practical application, which is the focus of the next section [54].

2.2.2 Exchange-Correlation Functionals

In practice, the use of the Kohn-Sham equations is related to the determination of of the exchange-correlation energy functional. The exact form of E$_{xc}$ is not known for any arbitrary density $\rho(\mathbf{r})$ and furthermore its derivation would require an incredible amount of algebra. To this end, approximate functionals based upon the electron density to represent this term, are presented. By now there is an endless list of approximating functionals that has had a large and still rapid expanding in field of research. In this thesis we review two popular approximations (in various forms) in use: the local density approximation (LDA) and the generalised gradient approximation (GGA).

(a) The local-density approximation (LDA)

This approach is based on the uniform electron gas. If we consider a real inhomogeneous system is divided into element volume d**r**, the electron density in each volumes is taken to be constant. In the LDA, the exchange correlation energy per electron from each volume, is taken to be the value it would have if the whole of space were filled with a homogeneous electron gas with the same density as is found in d**r** [56]. Thus, the E_{xc} of the system can be expressed as:

$$E_{XC}^{LDA}[\rho] = \int \rho(\mathbf{r})\epsilon_{XC}^{unif}\rho(\mathbf{r})d\mathbf{r} \tag{2.24}$$

where ϵ_{XC}^{unif} is the exchange-correlation energy per particle of the interacting uniform electron gas of density $\rho(\mathbf{r})$. Pratically, exchange and correlation terms are estimated separately. This term for the homogeneous electron gas is known analytically and is given by

$$E_{XC}^{LDA}[\rho] = -\frac{3}{4}\left(\frac{3}{\pi}\right)^{\frac{1}{3}} \int \rho^{\frac{4}{3}}(\mathbf{r})d\mathbf{r} \tag{2.25}$$

The exchange-correlation energy for the homogeneous electron gas has been calculated by fitting to the many-body studies of Gell-Man and Brueckner and Ceperly and Alder [57] or modern modifications such as that by Perdew-Zunger (PZ) [58], Perdew-Wang (PW) [59] and Vosko-Wilk-Nusair (VWN) [60]. Certainly, the LDA is suitable for solid-state systems, where the electron density varies only slowly. In general Eq. (2.24) can be applied to the system such as atoms, molecules, and solids. In particular LDA gives surprisingly results, especially for metals. The systematic error cancellation, which underestimates correlation E_c and overestimates exchange E_x, gives an unexpectedly good values of E_{XC}^{LDA}. This result is a partial explanation for this success. However, recent studies have shown that LDA, in molecular systems, often overestimates bonding energies and underestimates bond lengths [61]. In metals and insulators [62, 63], tends to overestimate cohesive energies by $\sim$ 15-20% and underestimates lattice constants by $\sim$ 2-3% . In other hand, for systems where the density varies slowly, the LDA tends to perform well, at the contrary in strongly correlated systems is very inaccurate [56].

(b) The generalised gradient approximation (GGA):

It is widely proven that only the local uniform density at each given point is not a satisfactory approximation for many materials where the electron densities rapidly varies. To address this deficiency and complement the information obtained by the LDA, the gradient of the density $\nabla\rho(\mathbf{r})$ needs to be included. One first attempt was expanding the exchange correlation parameter in function of the magnitude of the gradient of the density this was the so-called gradient-expansion approximations (GEA). The major drawback of the GEA could be explained by the fact that the gradient in real materials is so large that a given gradient expansion would break down. Indeed, higher-order corrections are exceedingly difficult to calculate and never improve the results in LDA, rather often even worsen it [64]. By eliminating the spurious long-range term of the second order expansion of the GEA exchange-correlation hole, one could apply more general functions of $\rho(\mathbf{r})$ and $\nabla\rho(\mathbf{r})$. Thus, the generalized gradient approximations known as GGAs were created and the corresponding exchange correlation energy, were approximated by:

$$E_{XC}^{GGA}[\rho] = \int f^{GGA}(\rho(\mathbf{r}), \nabla\rho(\mathbf{r}))d(\mathbf{r}) \tag{2.26}$$

GGAs depends on $\nabla\rho(\mathbf{r})$ and for this are often called "semi-local" functionals. As a general trend, GGAs yield more accurate results than the LDAs, for many properties, for example geometries and ground state energies of molecules and solids, where there are significant local variations in the electron density. Furthermore for covalent bonds, weakly bonded systems and the underestimation of bulk constant, many GGAs provide a better description than LDA. The GGA functionals remain computationally cheaper than some functionals found at higher levels of the so-called Jacob's ladder of functionals [65]. The functional form of f^{GGA} appearing in Eq. (2.26) is considered as a correction to the LDA exchange and correlation while guaranteing consistency with known sum rules. Within GGA the exchange energy takes the form

$$E_{X}^{GGA}[\rho] = \int \rho(\mathbf{r})\epsilon_{X}^{unif}(\rho(\mathbf{r}))F_{X}^{GGA}(s)d(\mathbf{r}) \tag{2.27}$$

where

$$s = \frac{|(\nabla\rho(\mathbf{r}))|}{2k_F\rho} \tag{2.28}$$

is the measure of inhomogeneity. Here $k_F = (3\pi^2)^{\frac{1}{3}}\rho(\mathbf{r})^{\frac{1}{3}}$ is the Fermi wave vector for homogeneous electron gas with density ρ. $F_X^{GGA}(s)$ is the exchange enhancement factor and describes how much exchange energy is improved over its LDA value for a given $\rho(\mathbf{r})$. One GGA differ from another in the choice of F_X.

$$s = \frac{|(\nabla\rho(\mathbf{r}))|}{2(3\pi^2)^{\frac{1}{3}}\rho(\mathbf{r})^{\frac{4}{3}}} \tag{2.29}$$

The $F_X(s)$, widely used GGA exchange functional, applied in this thesis is the one developed by Perdew-Burke-Ernzerhof (PBE [66]). It is a simplified construction of GGA for exchange and correlation, in which all parameters are fundamental constants.

The PBE functional takes the form:

$$F_s^{PBE} = 1 + \kappa - \frac{\kappa}{1 + \mu^2 s/\kappa} \tag{2.30}$$

where μ=0.21951 and κ=0.804 are obtained from physical constraints (non-empirical). The functional form to the gradient corrected correlation energy E_c^{GGA} is also expressed as complex function of s. Some of the common GGA functionals include those of Perdew, Burke, and Ernzerhof (PBE) [66], PW91 [67] Lee-Yang-Parr (LYP [68]), and Perdew86 (P86 [69]). The exchange and correlation functional most successfully employed in many surface physics studies, including this thesis, is the GGA-PBE.

2.3 Basis set and Pseudopotentials

In this paragraph, are introduced the concepts of basis set and of pseudopotentials. In practical, the use of basis sets are almost always required to solve the electronic Schrödinger equation. Nowadays a numerous amount of basis set representations is known and available and almost all electronic structure methods today rely on an expansion on the unknown wave function in terms of a set of basis functions. However, any kind of basis function electrons may in principle be used like exponential, Gaussian, polynomial, plane-wave, spline, Slater type orbitals, and numeric atomic orbitals, etc. [48] In develop a universal basis set, some issues are useful to consider when selecting basis functions:

- The basis functions should represent for the wave function/density with high accuracy and with a low computational effort
- The typology of the basis functions choice will ideally capture some of the physics of the problem.

The calculation of electronic-structure properties within Density-Functional Theory (DFT) for periodic systems, are carried out with Plane-Wave basis set and pseudopotentials.

In a condensed matter, for the treatment of periodic systems, like solids, the solution to the Kohn-Sham equations would not be possible without the explicit use of periodicity and the approximations assumed therein. The plane wave basis sets have become the natural choice because of Bloch's theorem [70, 71] which includes the use of periodic boundary conditions.

In a perfect crystalline solid, the atomic ions will produce a periodic potential, U($\mathbf{r}$) The periodicity of the potential U($\mathbf{r}$) will correspond to the periodicity of the Bravais lattice., where U($\mathbf{r}+\mathbf{R}$) = U($\mathbf{r}$) and $\mathbf{R}$ is the Bravais lattice vector. Bloch's theorem argues that the eigenfunctions of the one-electron Hamiltonian in a periodic potential H $= -\frac{1}{2}\nabla^2 + U(\mathbf{r})$ can be expressed as the product of a plane wave ($e^{i\mathbf{kr}}$) and a periodic function $\mu_{n,k(\mathbf{r})}$ with the periodicity of the crystal lattice:

$$\phi_{n,k}(\mathbf{r}) = e^{i\mathbf{kr}}\mu_{n,k}(\mathbf{r}) \tag{2.31}$$

Where $\mu_{n,k}(\mathbf{r}+\mathbf{R}) = \mu_{\mathbf{n},\mathbf{k}}(\mathbf{r})$ for all R in the Bravais lattice. Here, k represents a set of plane waves within the reciprocal space unit cell and the quantum number n represents the band index that occurs because of the many independent eigenstates for a given k. The Bloch's theorem, allow to solve the problem of the infinite number of electrons expressing the wavefunction in terms of an infinite number of reciprocal space vectors within the first Brillouin zone of the periodic cell. By use of Bloch's theorem, the electronic wavefunction are now expressed at each **k** points in terms of a discrete plane wave.

Therefore, in order to calculate the properties of a periodic crystal which contains electrons in the order of Avogadro's number, the spacing of the **k** points goes to zero and **k** can be considered as a continuous variable. In case of an infinite crystal, the number of electrons within the solid gives rise to an infinite number of **k** points, and at each **k** point only a finite number of electronic states are occupied. The physical quantities such as the electronic potential, electron density, and total energy of the solid are then defined via a discrete sum over eigenenergies in **k**-space However, one does not need to consider all of these **k** points, in fact, the electronic wave functions at **k** points that are very close together will be almost identical. Hence it is possible to represent them over a region of **k** space only by considering the wavefunction at a single **k** point. Valid methods have been devised to choose special finite sets of **k** points, in order to determine the groundstate density of the solid. In order to facilitate the calculations, an unbiased method of choosing a set of **k** points for sampling the Brillouin zone is a Monkhorst-Pack grid [72], in which a uniform mesh of **k** points is generated along the three lattice vectors in reciprocal space. The crucial point for the convergence of the results, is the choice of the **k** point mesh. To this end, convergence tests with respect to the density of **k**-points are necessary. Due to the periodicity of a crystal, the function $\mu_{n,k(\mathbf{r})}$ with plane waves whose wave vectors are reciprocal lattice vectors ($\mathbf{G}$) of the periodic crystal:

$$\mu_{n,k}(r) = \sum_{G} C_{n,\mathbf{G}} e^{i\mathbf{G},\mathbf{r}} \tag{2.32}$$

so the electronic wave function can be **expressed** in the following form:

$$\phi_{n,k}(\mathbf{r}) = \sum_{G} C_{n,k+\mathbf{G}} e^{i(\mathbf{k}+\mathbf{G})} \tag{2.33}$$

If we consider the Kohn-Sham equation (2.19) and replace Kohn-Sham wave functions expanded with plane wave basis sets as described in Eq. (2.38), we obtain the one electron Schrödinger-like equation of a periodic crystal with a plane wave basis set defined by:

$$\sum_{G} \left[\frac{1}{2} |\mathbf{k} + \mathbf{G}'|^2 \delta_{G,G'} + V^{eff}(\mathbf{G} - \mathbf{G}') \right] C_{n,\mathbf{k}+\mathbf{G}'} = \epsilon_n C_{n,\mathbf{k}+\mathbf{G}} \tag{2.34}$$

where $\delta_{G,G'}$ is the Kronecker δ indicating the orthogonality of the plane waves basis set, ϵ_n are the electronic energies and $\mathbf{G}'$ indicate that is necessary an infinite number of plane waves to solve Eq. (2.34) Furthermore, the coefficients $C_{n,k+\mathbf{G}}$ for the plane waves with small kinetic energy are typically more important than those with large kinetic energy. Thus the plane wave basis set can be truncated to include only plane waves that have kinetic energies less than a particular energy cutoff E_{cut},

$$\frac{1}{2} |\mathbf{k} + \mathbf{G}|^2 \leq E_{cut} \tag{2.35}$$

Employing a finite basis set introduces a new source of in accuracy, which can be reduced by increasing the number of plane waves or E_{cut}. Therefore, appropriate convergence tests have to be performed in order to find an E_{cut} that is sufficiently converged to compute the property of interest with the required accuracy [73, 74, 48, 75]. It is well known that most physically interesting properties of materials are largely dependent by the electrons in valence region, i.e. those coming from outer atomic shells, rather than the electrons in core region, those coming from inner atomic shells. The treatment of core electrons require a an extremely large number of plane waves to accurately describe the deep potential near the nuclei and produce a vast amount computational time to calculate the electronic wave functions. To this reason, the pseudopotential approach formalizes the neglect of core electrons. Computational times can be greatly reduced by the utilization of the so-called pseudopotentials (PSs) replicating the strong ionic potential with a weaker pseudopotential. In practical, the pseudopotential approximation has two main purposes to take into account: (i) to avoid the direct consideration of the less important core electrons in the bonding process (ii) to eliminate the rapid oscillations of the valence electron wave functions in the core region. In other hand, it is appropriate to attempt to replace the strong Coulomb potential and core electrons by an effective pseudopotential which is much weaker than the all-electron one and replace the valence electron wave-functions, which oscillate rapidly in the core region, by pseudo-wave-functions. In Fig. (**??**) is shown as the pseudopoential is much weaker than the all-electron one and that the pseudo wave function has no radial node inside the core region. It also becomes crucial that outside core region, the pseudo potential and wave function becomes identical with the corresponding all-electron ones [76, 56, 74].

Two important class of pseudopotentials are so called $norm - conserving$ pseudo potentials (NCPPs) and $ultrasoft$ (USPPs) pseudopotentials. Norm conserving pseudopotentials produce nodeless valence wave functions which converge to become identical to normalised full-potential wave functions beyond a chosen core radius (r_c), and are themselves property normalised. This latter property is essential for producing a correct description of bonding in pseudo potential calculations, and correct self consistent electrostatic and exchange-correlation potentials. [77] There are many types of norm-conserving pseudopotentials from different authors such as Hamann, Schlu̇̈ter, and Chiang [78], Kerker [79], Troullier and Martins [80] and Goedecker-Teter-Hutter [81]. One issue with the norm-conserving pseudopotentials is that they can not generate smoother pseudo wave functions than the all-electron one when coming to the first row elements (in particular N, O, F) and and for transition metals, in particular the 3d row: Cr, Mn, Fe, Co, Ni, ...

To overcome the problem, Vanderbilt [82] in early 1990, made a radical modification to break the norm conservation rule and relax the condition that the pseudo wave function inside the core region must have the same charge (or integrated density) as the all-electron wave function. This modern pseudopotential are known as ultrasoft pseudopotentials. As the name suggests, ultrasoft pseudopotentials gain much softer pseudo-wavefunctions so use considerably fewer plane-waves for calculations of the same accuracy. Consequently, this offers greater flexibility in the construction of the pseudo-wavefunctions but introduces a deficit in the charge inside the core region due to the relaxation of the norm-conservation constraints. The compensation is attained by the introduction of atom-centered augmentation charges to ensure the proper density and potential. The additional charges are defined as the charge difference between the all-electron and pseudo wave functions and for convenience they are also pseudized [83]. The major advantages of ultrasoft pseudopotentials are: the gain in efficiency obtained by using a lower kinetic energy cut-off and a good scattering properties over a pre-specified energy range, which results in much better transferability and accuracy of pseudopotentials. The gain of USPPs is mitigated to an extent by the necessity of calculating more terms. USP usually also treats "shallow" core states as valence by including multiple sets of occupied states in each angular momentum channel [48, 84, 85]. This also adds to high accuracy and transferability of the potentials, although at a price of computational efficiency [86]. The combination of DFT with plane-wave basis set and pseudopotentials has become "the standard approach" for first-principles electronic-structure calculations of extended systems.

2.4 Many-Body perturbation theory: The GW approximation

The estimate of ground-state and excited-state properties of materials have been one of the major aim of condensed matter physics. Density functional theory provides a good description of ground state properties but the the energy to add or remove an electron to or from a system is often required. State-of-the-art calculations for materials are based on the many-body perturbation theory (MBPT) [87, 88].

Many-body perturbation theory is a convenient framework up to now for the calculation of electronic excitations of extended systems. The main ingredient is the electronic self-energy that, in principle, contains all many-body exchange and correlation effects beyond the Hartree potential. As its exact mathematical expression is unknown, approximations must be used in practical calculations.

The approximation is obtained using a systematic algebraic approach on the basis of Green function techniques. It constitutes an expansion of the self-energy up to linear order in the screened Coulomb potential, which describes the interaction between the quasiparticles and includes dynamic screening through the creation of exchange-correlation holes around the bare particles. The implementation of the approximation relies on a perturbative treatment starting from density functional theory [87].

As for a system of non-interacting electrons, these energies correspond to the one-electron energies, while for a system of interacting electrons, the KS system can be used to calculate the ground state energy, but no theorem links the KS one-electron energies to the electron addition and removal energies. [90] These processes are accessible to direct/inverse photoemission spectroscopies and can be described theoretically in terms of quasiparticle QP spectra. In other hand, a system of quasiparticles that interact via the non-local and energy-dependent self-energy Σ should be considered. The fundament of the resulting quasi-particle equations is provided by many-body perturbation theory [87, 88].

The application of MBPT to the simulation of materials is plagued by severe numerical difficulties, which have limited so far these applications to models of a few handfuls of non-equivalent atoms, at most. The two main such difficulties are the necessity to calculate and manipulate large matrices representing the charge response of the system electron polarizabilities or polarization propagators [91], on the one hand, and that of expressing such response functions in terms of slowly converging sums over empty one-electron states. Umari et al [92] have successfully addressed the first problem by expressing polarizability operators in terms of an optimally small set of basis functions [91] and hopefully solve, the second problem to calculate polarizability operators and self-energy operators, based on a Lanczos-chain technique, inspired by recent progresses in time-dependent density-functional perturbation theory [93, 94]. Moreover, they explain how also optimal basis sets for representing polarizability matrices can be obtained without calculating empty states.

Quasi-particle energies (QPE) are eigenvalues of a Schrödinger-like QP equation (QPEq) for the so-called QP amplitudes (QPA). This energies are obtained from the solution of an equation similar to the Kohn-Sham one, but with the KS exchange-correlation (xc) potential Vxc replaced by non-local, energy-dependent, and non-Hermitian self-energy operator, where Σ is equal to the product of the one-particle Green's function G and the screened Coulomb interaction W. The next level of approximation is the GWA [95] which is the product of the one-electron propagator, G (Green's Fuction), and of the dynamically screened interaction, W:

$$\Sigma_{GW}(\mathbf{r},\mathbf{r}';\omega) = \frac{i}{2\pi}\int_{-\infty}^{\infty} d\omega' G(\mathbf{r},\mathbf{r}';\omega')W(\mathbf{r},\mathbf{r}';\omega-\omega') \tag{2.36}$$

The GWA alone does not permit to solve the QPEq, unless G and W are known, possibly depending on the solution of the QPEq itself. One of the most popular further approximations is the so-called G_0W_0 approximation G_0W_0A [96], where the one-electron propagator is obtained from the QPEq using a model real and energy-independent self-energy, and the irreducible polarizability P is calculated in the random-phase approximation (RPA)

$$P(\mathbf{r},\mathbf{r}';i\omega) = 4Re\sum_{cv}\frac{\psi_c(\mathbf{r})\psi_{\mathbf{v}}(\mathbf{r}')\psi_{\mathbf{v}}(\mathbf{r})\psi_{\mathbf{c}}(\mathbf{r}')}{i\omega-(\epsilon_c-\epsilon_v)} \tag{2.37}$$

where ψ and ϵ are zeroth order QPAs and QPEs and ν and c suffixes indicate occupied and empty states, respectively.

In order to substantially reduce the computational load, Umari et al. [91, 92] proposed an optimal representation identified in two steps: (i) they first expressed the Kohn-Sham orbitals, whose products enter the definition of P°, in terms of localized, Wannier-type, orbitals; (ii) then constructed a basis set of localized functions for the manifold spanned by products of Wannier orbitals, such that their norm is larger than a given threshold. They expressed valence and conduction QPAs in terms of localized, Wannier-type, orbitals and then reduced the number of product functions necessary to represent the $\Psi's$ the product between the number of valence and conduction states, which scales quadratically with the system size, to a number that scales linearly. The resulting functions are no longer orthonormal. A minimal orthonormal basis is finally generated as above by diagonalizing the corresponding overlap matrix and retaining only those eigenvectors that correspond to eigenvalues larger than a given threshold. The advantage of passing to the Wannier representation is that this transformation reduces the number of significant eigenvalues of the overlap matrix and these matrix elements can be efficiently calculated by a Lanczos-chain algorithm [97] as explained in Ref. [94]. More details about many-body perturbation theory and applications are provided in the reviews Refs. [92, 91].

2.5 Gap correction

In the solid-state community, the vast majority of electronic structure calculations are done using the Kohn-Sham equations [55] with the local-density approximation (LDA) [59] or generalized gradient approximation (GGA) [66] for the exchange-correlation energy and potential. The principal account is that these (semi)local approximations yield, in many situations, results which are accurate enough to comprehend experimental data or to have some predictive power. Another important advantage of semilocal functionals is that they lead to calculations which are computationally cheap in comparison to more sophisticated methods. In any case, the employment of LDA and GGA to solids can also lead, depending on the studied solid and property, to results which are in very bad agreement with experiment, e.g., for the band gap of semiconductors and insulators which is severely underestimated or even absent (see, e.g., Ref. [98]) [99]. The gap underestimation in density functional theory is a well-known systematic error that can be corrected by solving the many-body perturbed Hamiltonian in the G_0W_0 approximation [100, 101]. Nevertheless, standard DFT-GGA ensures a correct order of electronic states. The underestimation may also occur in the case of deep defect-induced levels in the band gap, which leads to a question about the accuracy of both the energies of the defect-induced levels and of their formation energies obtained within LDA/GGA. More accurate band gap energies are obtained within the GW approximation, which shows that the errors mainly arise from the underestimation of the energies of conduction states [102]. The calculated values of the bandgaps of the II-VI compounds by these techniques are presented in Fig. 2.1. The comparison of the results obtained by these techniques with the experimentally measured values confirm that the errors in most of the calculated results are more than 10%, which is technically not acceptable in the scientific community [103]. In other words the first principles calculations based on many-body perturbation theory, such as the GW approximation, has been shown to be reliable for obtaining quasiparticle band gaps of semiconductors. In this thesis the G_0W_0 approximation was applied - as implemented in quantum ESPRESSO package [116] - in order to correctly estimate the band gap and the band edge positions in CdS. In particular, the band gap in bulk CdS was directly calculated while valence (VBM) and conduction (CBM) band edges in $[10\bar{1}0]$ CdS surface were evaluated according to the procedure suggested in Ref. [104] and illustrated in the following.

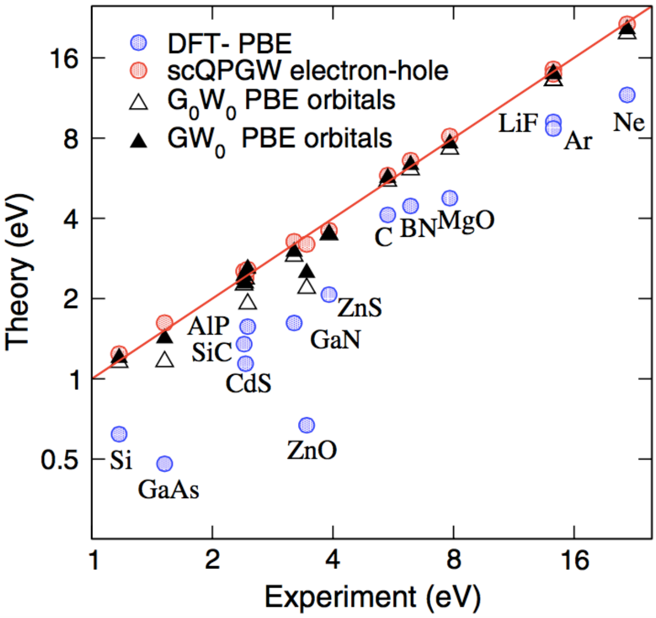

Figure 2.1: Illustrative comparison of band gaps done G_0W_0 and GW_0 and self-consistent quasiparticle GW (scQPGW) band gaps, along with results using the semilocal Perdew-Burke-Ernzerhof (PBE) functional. Reprinted picture from Ref.[1] Copyright © 2014, American Chemical Society.

In practice, the band energies computed with KS-DFT are shifted due to the contribution of the pseudopotential (which represents the potential due to the nuclei plus core electrons) at zero momentum vector when employing periodic boundary conditions [104, 105].

Therefore, the positions of KS eigenvalues with respect to the vacuum level can be obtained using a periodic cell model containing a slab representing a semi-infinite surface and a sufficiently thick vacuum region that eliminates interactions between slab periodic images [106, 104]. The work function ϕ, defined as the minimum energy required to extract an electron from a material, is equal to the energy difference between the Fermi level and the electrostatic potential energy in vacuum. The work function can also be described in terms of the VBM,

$$\phi = [E_{VBM} + \Delta] \tag{2.38}$$

where $\Delta = \frac{1}{2}E_g$ for an undoped material. Per convention, all electron energies are referenced to the potential energy in the vacuum region. Specifically, in slab models of semiconductors, the energy of the KS VBM equals the energy of the highest occupied band referenced to the potential energy in vacuum (the latter being set to zero energy as the reference state).

Thus, the VBM of a material is conventionally assumed in the literature to be equal to the KS VBM.[106, 107] The CBM may then be determined by adding an energy gap to the KS VBM. The energy gap is usually obtained either experimentally [107] or theoretically from, e.g., a quasiparticle (QP) gap calculation [108] This approach of calculating the VBM of a semiconductor from KS-DFT suffers from an error associated with the derivative discontinuity of the XC energy [109].

A theorem proved by Perdew and Levy [109] shows that DFT can only provide a lower limit to the absolute value of the VBM even if the XC functional used is exact, because of the inherent assumption in the KS formalism that the XC functional is energy independent. However, the theorem also shows that DFT is formally exact for calculating the band gap center (BGC), denoted here by E_{BGC}. Therefore, here we calculated the BGC based on Perdew and Levy's proof that extends to non-metallic systems Janak's theorem for calculating the work function [110, 104]. To determine the VBM and CBM from E_{BGC} the energy gap needs to be computed as well. Although many publications purport to predict band gaps from KS-DFT, such gaps are not directly related to any actual measurements. We refer instead to such gaps as eigenvalue gaps, since they are merely the difference in KS eigenvalues between the lowest unoccupied and highest occupied states. Because of the lack of derivative discontinuity in the XC functional mentioned above, among a host of other reasons, these KS eigenvalue gaps are not equivalent to either optical or photoemission/inverse photoemission (PES/IPES) gaps and any agreement quoted with respect to experiment is merely fortuitous. By contrast, the many-body Green's function theory known as the GW method has successfully calculated the QP gap of many semiconductor materials [104, 111]. The QP gap is essentially the ionization potential minus the electron affinity of the material, a quantity which is directly comparable to the gap measured by PES/IPES experiments. Finally, we corrected these band edges within an approximate G_0W_0 approach, as full GW calculations are prohibitively heavy for these complex surfaces. We thus combine E_{BGC}, obtained from the DFT calculation on the CdS surfaces, with the band gap E_g obtained from the G_0W_0 result on the bulk, to calculate the VBM and conduction band minimum (CBM), in the following manner [104]:

$$E_{VBM} = E_{BGC} - \frac{1}{2}E_g^{GW} \tag{2.39}$$

$$E_{CBM} = E_{BGC} - \frac{1}{2}E_g^{GW} \tag{2.40}$$

The band gap center E$_{BGC}$, located midway between the Kohn-Sham valence band maximum (E_{VBM}) and conduction band minimum (E_{CBM}) eigenvalues was calculated for the surface (periodic slab) unit cell, in according to:

$$E_{BGC} = \frac{E_{VBM} + E_{CBM}}{2} \tag{2.41}$$

The position of the E$_{BGC}$ relative to vacuum was obtained by taking the energy difference of the calculated electrostatic potential in the vacuum region and E$_{BGC}$ as obtained in Eq. (2.41). The energy of the electrostatic potential at the centre of the vacuum was taken as the reference (E = 0) level.

CHAPTER 3

Native defects in CdS bulk

In this Chapter we report the nature of point defects in cadmium sulfide and their influence on the electronic structure. After a characterization of bulk CdS, cation and anion single vacancies are investigated - in the neutral state of charge - in terms of electronic and geometrical structure. Particular emphasis is addressed to the analysis of the formation energies and the influence of structure relaxation on the electronic levels.

3.1 Points defects in semiconductor

A perfect crystal is an idealizzation, in fact all real materials contain imperfections or defects and the atoms arrangement do not reproduce the perfect crystalline model. There is also a fundamental physical reason why the crystal is imperfect. While a perfect crystalline structure may be preferred energetically, at least in the limit of low temperature, atoms are relatively immobile in solids and it is, therefore, difficult to eliminate whatever imperfections are introduced into the crystal during its growth, processing or use [112].

Of the many types of materials that are technologically important today, semiconductors require the greatest level of impurities control [113]. Crystal defects in semiconductor materials have strong influence upon many properties of crystals, such as strength, electrical conductivity, ferromagnetic behavior and play a very important role in the understanding of their electrical and optical properties. It should be noted that defects do not necessarily have adverse effects on the properties of materials, sometimes these features are commonly intentionally used to manipulate the mechanical properties of a material. Imperfections in crystalline solids by their dimension, can be classified into the following kinds:

- Zero-Dimensional (0-D) defects
- One-Dimensional (1-D) defects
- Two-Dimensional (2-D) defects
- Three-Dimensional (3-D) defects

The 0-D defects affect isolated sites in the crystal structure, and are hence called *point defects*. The 1-D defects are line defects and include dislocations and junctions of, at least, three grain boundaries (triple junctions). The 2-D defects are surfaces, such as the external surface and the grain boundaries along which distinct crystallites are joined together. The 3-D defects change the crystal pattern over a finite volume. Point defects are imperfections that occur when an atom is missing or is in an irregular place in the lattice structure. Among point defects, it is useful to distinguish *intrinsic defects* from *extrinsic defects*. Intrinsic or native defects in the crystal are created when an atom is missing from its regular atomic site, creating a *vacancy*, or when an atom belonging to the native crystal patters occupies an interstitial site where no atom would ordinarily appear, causing an *interstitialcy* (see Fig. 3.1). *Extrinsic defects*, are mostly originating from inclusions of foreign atoms (impurity). Because the interstitial sites in most crystalline solids are small (or have an unfavorable bonding

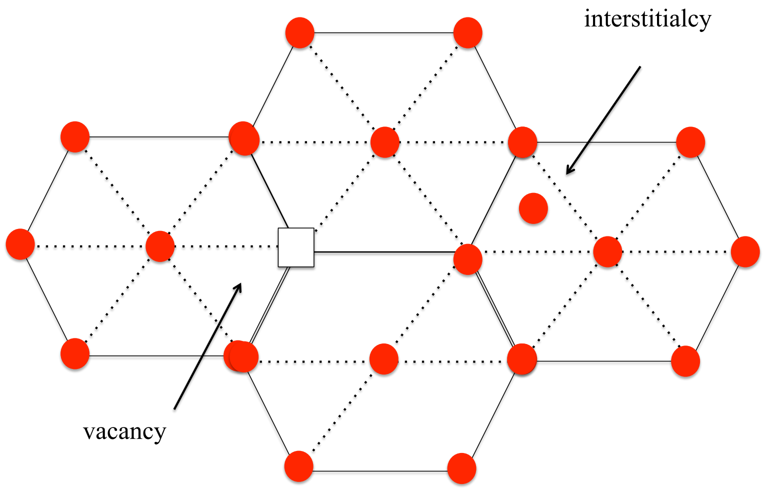

Figure 3.1: Illustration of a vacancy and an interstitial in a two-dimensional hexagonal lattice

configuration, as, for example, in the diamond lattice) they are generally high energy configurations and to this reason are relatively uncommon. Vacancies usually occur, in particular, at high temperatures when atoms frequently and randomly change their positions leaving behind empty lattice sites. In most cases the prominent effect in the presence of vacancies is the diffusion (mass transport by atomic motion). Defects assist the diffusion mechanism, which influences growth, processing, and degradation of any device. Thus several important properties of crystals are related to imperfections and also to the nature of the host materials.

In this thesis, based on first-principles calculations, we studied the influence of intrinsic defects on the electronic properties of CdS. In the specific case, we investigated the cation and anion single vacancies in the bulk and in the cleavage surface of CdS and the relationship between these defects and the trap states introduced in the band gap.

3.2 Trap states in CdS

Point defects in semiconductor materials strongly influence the physical properties of materials and have a decisive impact on their performance in applications. As a matter of fact, their presence create trap states in the band gap changing electrical and optical properties of the material. Extra levels in the gap typically associated with defects for which the local atomic geometry significantly deviates from the ideal bulk appear as localised. Examples of such defects include vacancies, interstitials, impurities with localised states only weakly interacting with the host. In general, deep levels energetically lie “deep” within the forbidden energy band [1, 114]. They generate bound states with well-localised wave functions (delocalised in k space). They can act as recombination-centers or killer-centers. The effects of deep levels are to drastically reduce minority carrier lifetimes and to act as traps for charge carriers.

Conversely, “shallow” levels are defect-induced states appearing closely above the VBM or below the CBM. Traditionally, shallow levels have been associated with substitutional atoms that have only a small impact on the crystal lattice and thus the bulk band structure, but which introduce extra hole/electrons into the system [1, 45]. Many important defects are electrically active. Defects which can contribute free electrons to the host crystal are known as donors, while defects which can contribute holes (i. e., remove free electrons) are known as acceptors [45].

Fig 3.2 reports a scheme of bands in semiconductors with the inclusion of extra levels, both donors (left) and acceptors (right).

The response to light in a pure semiconductor and with defects is different. When the semiconductors are irradiated, an electron is promoted from the valence band to the conduction band, leaving a hole behind. This electron-hole pair may recombine non-radiatively or radiatively by emitting light with energy slightly lower than the bandgap energy. The recombination of the electrons with holes in the trap states can also occur non-radiatively or radiatively [115]. The type of defects and the band edge emission can be expected to vary depending on the number and kind of traps as well as the competition between the radiative and non-radiative decay [39].

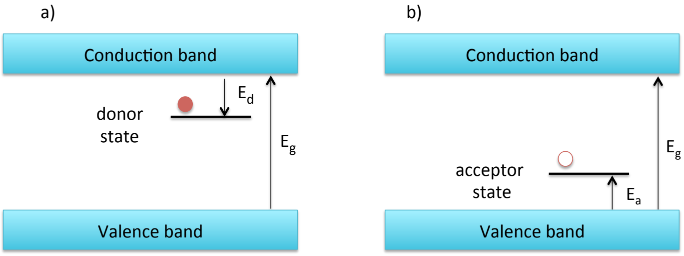

Figure 3.2: Schematic representation of energy levels in band-gap. (a) The donor levels are placed shortly below the conduction band edge. (b) The acceptor levels are placed just above the valence band.

In the specific case of yellow pigment we will refer to a semiconductor (CdS) that shows band edge luminescence in the visible range and deep traps luminescence in the red/infrared range possibly due to crystal defects. [34] A large body of experimental data, as described in 1.1.1, shows the presence of trap states in the gap of CdS compounds used as yellow pigments in modern paintings. Such traps will be discussed in some details in the following.

3.2.1 The vacancy formation energy in CdS

From thermodynamics the concentration of defects at equilibrium decreases exponentially with increasing defect formation energy. The formation energy is thus the foremost entity to be calculated, as it explicitly determines the concentration and the transition levels of the defect. In this section we show the procedure to calculate the formation energy of single vacancies in CdS. Anion and cation single vacancies both in bulk and $[10\bar{1}0]$ CdS surface were taken into account. In particular, we focus on the role of Cd- and S- vacancies in several non-equivalent positions. In the defective system the vacancy formation energy was calculated according to:

$$\Delta E^V = E^V - n_{Cd}\mu_{Cd} - n_S\mu_S \tag{3.1}$$

where E^V is the total energy of the supercell with a defect, n_X the number of X-th type of host atoms (X = Cd, S), μ_X the corresponding chemical potential obtained from separate calculations.

3.2.2 Chemical potentials

Chemical potentials depend on experimental growth conditions and are directly related to heat of formation (ΔH) which represents the energy gain in forming the crystal. In the case of CdS, the heat of formation ΔH_{CdS}, was obtained from the following equation:

$$\Delta H_{CdS} = \mu_{CdS} - \mu^0_{Cd} - \mu^0_S \tag{3.2}$$

where μ^0_{Cd} and μ^0_S are the elemental chemical potentials and μ_{CdS} is the chemical potential of cadmium sulfide in wurtzite phase that, at equilibrium, is represented by the sum of Cd and S chemical potentials:

$$\mu_{CdS} = \mu_{Cd} + \mu_S \tag{3.3}$$

In practice, μ_{CdS} was obtained as the total energy of the primitive unit cell per formula unit and the elemental chemical potentials μ^0_{Cd} and μ^0_S in Eq. 3.2 were given by total energy per atom of bulk Cd metal in the hcp structure and S_2 molecule in gas phase. Among all the possible processes in the pigment synthesis, there are two extreme growth conditions, namely S-rich or Cd-rich. In the first case, to simulate a S-rich growth condition $\mu_S = \mu^0_S$ while μ_{Cd} is obtained by a combination of Eq. 3.2 and 3.3: $\mu_{Cd} = \mu^0_{Cd} + \Delta H_{CdS}$. In S-rich the heat of formation resulted ΔH_{CdS} = -1.85 eV, in excellent agreement with that obtained in Ref [42]. Vice versa, in Cd-rich growth conditions, $\mu_{Cd} = \mu^0_{Cd}$ and $\mu_S = \mu^0_S + \Delta H_{CdS}$. The formation energy was calculated in both conditions.

Only neutral state of defect charge is here considered since charged vacancies are typically related to doped CdS that is not the scope of the present work.

3.3 Bulk CdS

The unit cell of wurtzite CdS is a hexagonal structure belonging to the space group P6$_3$*mc* and contains four atoms as shown in Fig. 3.3. To model the infinite bulk of wurtzite CdS, periodic boundary conditions were used. The lattice parameters, namely a and c/a were theoretically determined using the Density Functional Theory in the Generalized Gradient Approximation in the (DFT-GGA PBE) as described in 2.2. To this end, the suite of codes implemented in the package quantum-ESPRESSO [116] was used. For reasons that will be clear in the following sections, both ultrasoft (US) [82] and norm-conserving (NC) [117] pseudopotentials (PP) were employed.

The Kohn-Sham equations were solved by using a plane waves basis set and the kinetic energy cutoffs for the electron wavefunctions as large as 90 Ry in the case of NC-PP while 28 Ry and 280 Ry for electron wavefunctions and augmented electron density, respectively, in the case of US-PP. Valence electron configurations included Cd $5s^2$ $5p^2$ $4d^{10}$ and S $3s^2$ $3p^4$. The Brillouin zone sampling was performed with a Monkhorst-Pack sampling with a mesh of $4 \times 4 \times 4$ k-points. In order to confirm the stability of CdS in wurtzite phase [118] as opposite to the zincblende cubic one the cohesive energy E_{coh} was calculated for increasing volumes. The cohesive energy E_{coh} was obtained from energy-volume curves fitted by means of Murnaghan's equation of state [119]. E_{coh} was calculated according to:

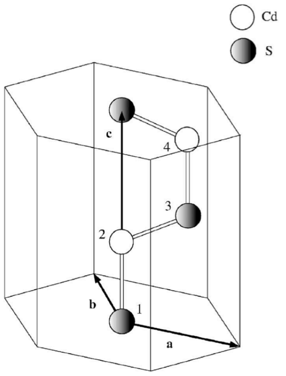

Figure 3.3: Primitive unit cell of wurtzite CdS with four atoms labeled 1-4 at positions (0, 0, 0) and (0.667, 0.333, 0.5) and S-atoms at (0, 0, u) and (0.667, 0.333, u + 0.5), where u= 0.377 is cell internal structural parameter is also close to the experimental value of 0.373. The lattice vectors are $v_1 = a(1,0,0)$, $v_2 = a(-1/2,\sqrt{3}/2,0)$, $v_3 = a(0,0,c/a)$ [2].

$$E_{coh} = \frac{E_{CdS} + [nE_{Cd} + nE_S]}{n_{pairs}} \tag{3.4}$$

where E_{CdS} is the total energy of CdS in wurtzite o zincblende phase, E_{Cd} and E_S are the total energies of isolated elements and n_{pairs} is number of CdS pairs in the simulation cell.

The result is summarized in Figure 3.4. The E_{coh} in wurtzite is slightly lowest that in zincblende with ΔE_{coh}= -0.04 eV and the values for both structures are in a good agreement with other theoretical results (ΔE_{coh}= -0.08 eV) [120].

The theoretical lattice parameters minimizing the two curves are listed in Table 3.1. They agree quite well with experiments and other the theoretical results obtained with a similar approach [2]. Figure 3.5 shows electronic band structure and density of states (DOS) of wurtzite CdS.

On the left side the band structure reveals a direct energy gap at Γ, as expected. The calculated Kohn-Sham energy gap E_g^{DFT} resulted as large as 1.65 eV, smaller

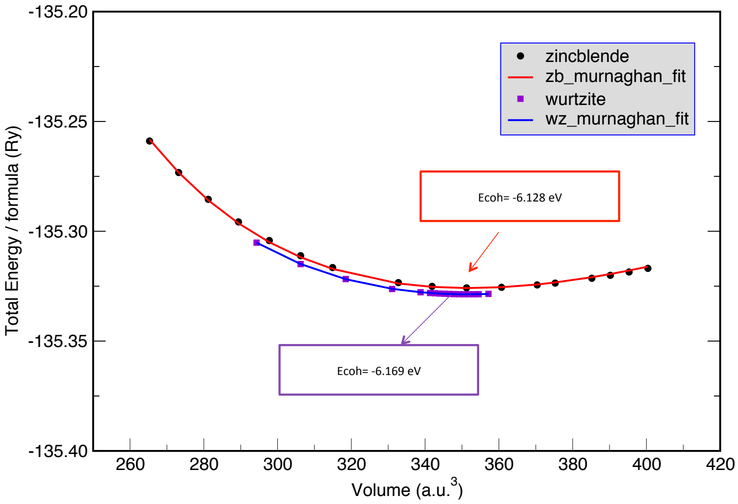

Figure 3.4: The total energy/formula versus volume of cell for CdS in zincblende and wurtzite phase

Table 3.1: Optimized structural parameters of wurtzite CdS

	a (Å)	c (Å)	c/a	μ
US-PP Present work	4.20	6.83	1.63	0.376
NC-PP Present work	4.19	6.81	1.62	0.376
others [2]	$4.20^{a,b}$	6.83^{a} 6.85^{b}	$1.63^{a,b}$	0.377^{a} 0.375^{b}
Δ% our-exp	1.44-1.20	1.78-1.33	0.61	0.80
exp. [121]	4.14	6.72	1.62	0.373

[a] Reference [2] [b] Reference [120]

than the experimental value E_g^{exp}=2.42 eV measured in wurtzite CdS [122, 70]. The gap underestimation in density functional theory is a well-known systematic error that will be corrected by solving the many-body perturbed Hamiltonian in the G_0W_0 approximation. [111]. The DOS (right side) shows the typical profile of hexagonal CdS. It presents in the lower band at around -8 to -6 eV the Cd *d*-states and the small contribution of S *s*-state. The valence band between -4 eV and Fermi level is mostly derived from the S *p*-states and the lowest conduction band mainly from Cd *s* states. The Cd *4d*-states are explicitly accounted for in calculates. Our calculated DOS is in general good agreement with other theoretical results [2].

As already mentioned, the Kohn-Sham gap was corrected by performing a GW calculation according to the method proposed in ref. [91, 92]. To this end several convergence tests were performed to optimize typical parameter needed for the calculation, namely the polarizability basis and the cutoff. The results of such tests are plotted in Fig. 3.6 where the calculated energy gap E_g^{GW} is represented as a function of the

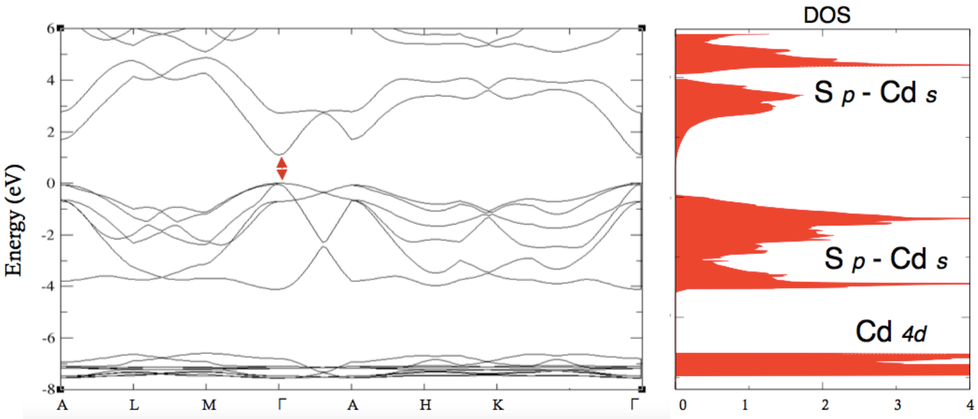

Figure 3.5: Band structure calculated for wurtzite CdS (left hand site) and corresponding density of states (right-hand side). The valence-band maximum has been placed at the zero of the energy scale. The letters A-Γ and denote high-symmetry points in the first Brillouin zone

length of the polarizability basis for several values of the cutoff for the plane-waves. Final optimal parameters were 5 Ry for plane wave cutoff and 600 for the length of the polarizability basis. The corrected gap energy is finally $E_g^{GW} = 2.38$ eV.

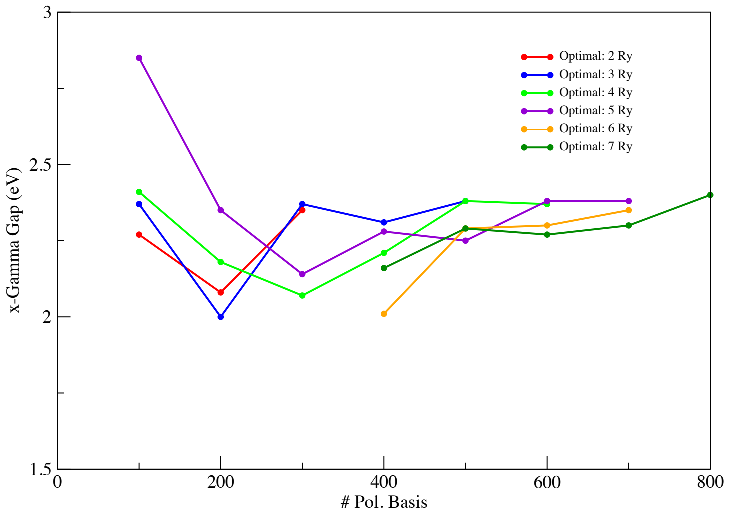

Figure 3.6: Convergence of E_g^{GW} is represented as a function of the polarizability basis corresponding to the respective cutoff energy.

3.3.1 Cation vacancy

To explore the electronic structure of wurtzite CdS with S and Cd vacancies in neutral state, we performed a series of calculations using a supercell consisting of 4x4x2 wurtzite CdS primitive unit cells, which contains 128 atoms. The use of a large hexagonal supercell considerably reduces the defect-defect interactions that arises from the interaction with periodic images.

For CdS in wurtzite phase each cation(anion) is tetrahedrally coordinated with an anion(cation). Furthermore, each ion has twelve next-nearest neighbors of the same type. The formation of a vacancy in the bulk implies the generation of four dangling bonds, one each on the adjacent atoms, which tend to form states at the position of the original sp^3 hybrid.

Here, a cation vacancy V_{Cd}, was generated by removing one Cd atom from supercell. The whole system was then allowed to relax until the residual atomic force became less than 10^{-4} eV/$\AA$. As a result of the relaxation, the four nearest-neighbors (NN) S atoms move inward into the vacancy site as well as the next-nearest neighbors (NNN) Cd atoms. The different distances are shown in Table 3.2 where the first column reports the distance calculated in the ideal structure while in the second column relaxed distances are listed. The third column represents the variation in percentage of the two abovementioned distances. The minus sign indicates henceforth a contraction of bond-lengths as opposite to an expansion indicated with a positive sign. The initial site of the vacancy is assumed to be on the ideal site of the removed atom. The geometry of the structure is depicted in Fig. 3.7 (left) where the red bonds are a guide for the eye to highlight the distances between nearest neighbors and the vacancy site. The corresponding density of states was calculated and plotted in Fig. 3.7 (right) where red and green curves indicate the spin-up and spin-down contributions compared to the ideal system (grey shaded). The presence of V_{Cd} is remarked in the spin-down contribution where a peak is in the valence band close to VBM, the latter set as the Fermi level ($E_F = 0$), is visible. Notice, the peak close to the Fermi

Table 3.2: Cd vacancy: distances between NN and NNN and the defect site before and after the relaxation. Corresponding variation distances ($\Delta d\%$) are included.

defects	ideal (Å)	relaxed (Å)	$\Delta d\%$
d[V_{Cd} - S (NN)]	2.44	2.57	-4.83
	2.51	2.56	-1.80
	2.49	2.56	-2.83
	2.50	2.56	-2.41
d[V_{Cd} - Cd (NNN)]	4.17	4.16	0.26
	4.12	4.19	-1.75
	4.12	4.23	-2.49
	4.10	4.20	-2.41

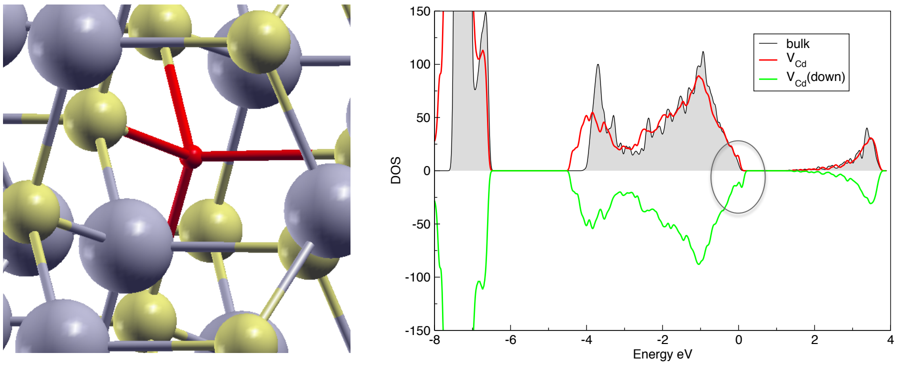

Figure 3.7: Left: Relaxed geometry of CdS bulk with V$_{Cd}$. The vacancy surrounding bonds are shown in red. Right: Calculated total DOS for V$_{Cd}$ including spin-up (solid green-red lines) compared to the CdS perfect bulk DOS in grey.

level (see grey circle in Fig. 3.7) represents occupied states and is mainly due to the contribution of under-coordinated S atoms (dangling bonds). As for the different spin contribution, there are several evidences [123, 124] showing that cation vacancies in CdS zincblende, can produce local magnetic moments. While several studies on vacancies in zincblende CdS are, in fact, reported in the literature, results for wurtzite CdS are very poor. In Ref. [123] a total magnetic moment was found as large as 1.778 μ_B for zincblende CdS, with an order of magnitude comparable to 1.58 μ_B obtained in the present work for V$_{Cd}$ in wurtzite CdS.

The vacancy formation energy ΔE_V was calculated both for ideal and relaxed structure according to the Eq. 3.1. Results obtained in different environment conditions, namely Cd-rich and S-rich (see Section 3.2.2) are in Table 3.3. Only one study [42] on point defects in wurtzite CdS reports $E_V = 2.26$ eV obtained in S-rich conditions that results in very good agreement with our result.

Table 3.3: Vacancy formation energies ΔE^V(eV) bulk in S-rich and Cd-rich conditions.

ΔE^V	S-rich	Cd-rich
V$_{Cd}$	2.25	4.12

3.3.2 Anion vacancy

In analogy with the procedure adopted for cation vacancy, we created a single sulfur vacancy V_S by removing one S atom from the pristine 4x4x2 wurtzite CdS containing 128 atoms. Again, the entire system was allowed to relax. The presence of V_S counts four dangling bonds due to the four nearest neighbors (NN) Cd. Upon geometrical optimization, the local geometry around the vacancy, changes significantly. The four Cd nearest neighbors (NN) move inward into the vacancy site as well as the next-nearest neighbors (NNN). This displacement of atoms is remarkable around V_S especially for three of the Cd-NN's (see atoms in green in Fig. 3.8, left), that come very close to each other with a decrease of their distances from 4.21Å to 3.20Å and 4.20Å to 3.15Å. Three new Cd-Cd bonds of 3.20Å, 3.15Å and 3.16Å respectively, are created. The relevant lattice deformation around V_S vacancy was also found by Nishidate et al. [2]. They ascribed this behavior to a strongly localised orbital at the vacancy site that attracts the neighboring positive Cd ions by the electrostatic force with a consequent inward lattice deformation. The calculated distances are shown in Table 3.4 where the first column reports the distance calculated in the ideal structure while in the second column relaxed distances are listed. The third column represents the variation in percentage of the two distances mentioned before. The rearrangement of the structure around the vacancy is illustrated in Fig. 3.8 (left) where the red bonds indicate the distances between NN and the vacancy site. The corresponding density of states was calculated and reported in Fig. 3.8 (right) where red curve is the total DOS of the bulk containing V_S compared to the ideal system (grey shaded). The presence of V_S did not lead to significant features in the electronic structure at least close to the band edges.

Table 3.4: S vacancy: distances between NN and NNN and the defect site before and after the relaxation. Corresponding variation distances ($\Delta d\%$) are included.

defects	ideal (Å)	relaxed (Å)	$\Delta d\%$
d[V_S - Cd (NN)]	2.56	2.04	-20.31
	2.57	3.05	+18.68
	2.56	1.99	-22.26
	2.57	2.01	-21.79
d[V_S - S (NNN)]	4.19	4.23	+0.95
	4.23	4.04	- 4.49
	4.22	3.98	-5.68
	4.22	4.16	-1.42
	4.21	4.01	-4.75

The vacancy formation energy ΔE_V was calculated for relaxed structure and the results obtained in both conditions Cd-rich and S-rich are listed in Table 3.5, where results for Cd vacancies are also reported for comparison. The formation energies obtained for both vacancies in S-rich conditions are in excellent agreement with a similar study [42] on S and Cd vacancies in bulk CdS obtained under the same conditions.

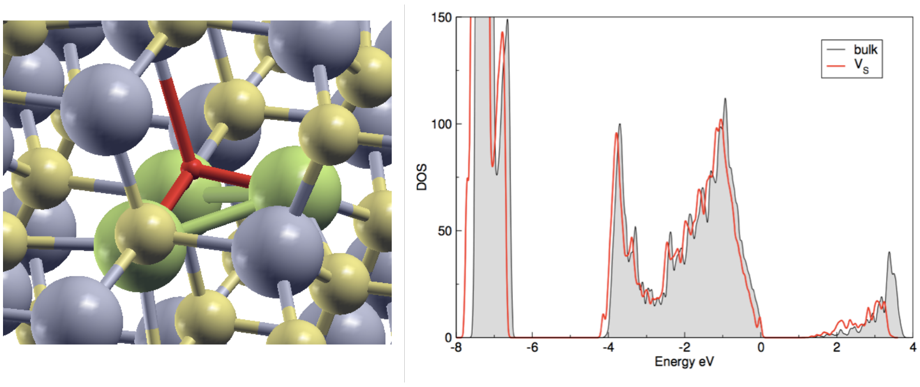

Figure 3.8: Left: Relaxed geometry of CdS bulk with V_S. The vacancy surrounding bonds are shown in red. Right: Calculated total DOS for V_S (solid red line) compared to the CdS perfect bulk DOS in grey.

In fact, they found 2.26 eV and 3.34 eV for Cd and S vacancies, respectively.

As for the overall picture of defect levels in the fundamental gap, the present work is also in very good agreement with previous theoretical studies [125, 126]: in relaxed wurtzite structure the Cd vacancy induces bound states inside the gap, while S vacancy gives rise to levels just below the conduction band minimum. The former refers to deep double acceptors while the latter are predicted to create shallow double donors.

Table 3.5: Vacancy formation energies ΔE^V (eV) bulk in S-rich and Cd-rich conditions. The values for V_{Cd} are also reported for comparison.

ΔE^V	S-rich	Cd-rich
V_S	3.20	1.33
V_{Cd}	2.25	4.12

CHAPTER 4

Native defects in [10$\bar{1}$0] CdS surface

In this chapter, a brief overview of the clean [10$\bar{1}$0] surface is first presented. The case of CdS [10$\bar{1}$0] surface with two non-equivalent vacancies for both cadmium and sulfur is next taken into account. We will refer henceforth to Cd vacancies as V_{Cd}^{top} and V_{Cd}^{hollow} and to S vacancies as V_{S}^{top} and V_{S}^{hollow}. The influence of such points defects on the electronic and geometrical properties of the surface are explored. A periodic 2x1 [10$\bar{1}$0] surface is used first as a benchmark. It allowed us to have a general overview of the behaviour of this defective surface and then a 2x2 surface of the same simmetry was adopted. For each system we calculated the formation energies in both Cd-rich and S-rich conditions. The analysis of the electronic structure was performed through the density of states and the bonding charge analysis. The band edges, namely the valence band maximum (VBM) and conduction band minimum (CBM) are corrected by referring them to the band gap center (BGC), to the electrostatic potential in the vacuum region and to the band gap calculated via the GW method.

4.1 Geometry of surface

The starting geometry of the surface was cleaved on the basis of the optimised hexagonal (wurtzite) structure along the direction perpendicular to the [10$\bar{1}$0]. The bulk structure parameters used to build the starting geometry of the supercell are listed in Table 3.1 (Sec. 3.3). The Brillouin zone sampling was performed with the same density of special k-points, 4x4x1, used in the bulk calculations. The use of a gamma-point-centered grid was important for determining the BGC in a material

with a direct band gap such as CdS. The surface structures were constructed using two-dimensional periodic slabs in the $x-y$ plane, comprising 2x1 and 2x2 supercells containing 40 and 160 atoms, respectively. In both cases, a slab containing 5 atomic layers was sufficient to represent the CdS [$10\bar{1}0$] surface since increasing the number of layers up to 7 layers both the surface energy and the interatomic distances showed no remarkable changes. 20Å of vacuum region separated the image-slabs in the $z-$direction to avoid any interactions due to periodic boundary conditions.
As for the clean surface, all the atoms were allowed to relax. This surface is nonpolar - i.e. equal numbers of surface anions and cations - and the structure of the relaxed CdS [$10\bar{1}0$] surface showed a characteristic ridged profile: the under-coordinated Cd cations relaxed inward, toward the bulk, whereas the under-coordinated S anions relaxed outward. toward the vacuum. (see Figure 4.1). The positions of the atoms in outermost layer are defined in terms of lateral distances *(D)* in either x or y directions parallel to the surface and interlayer distances perpendicular to the surface ($\perp$).

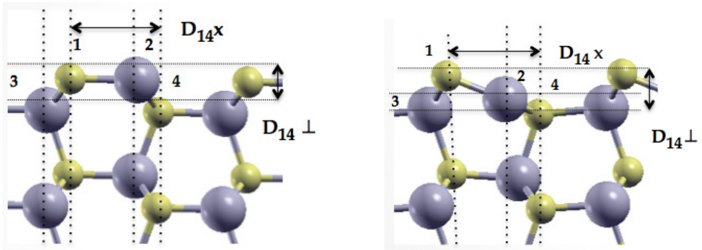

Figure 4.1: Side view of the ideal (left) and relaxed (right) configuration of the CdS [$10\bar{1}0$] surface. Distances $D_{1,4}$x and $D_{1,4}\perp$ are meant to be the distances between the atom 1 and the atom 4 along the x direction and the z direction, respectively. The complete set of calculated values is given in Table 4.1 in comparison with the results of Barnard and collaborators.[3]

In Table 4.1 are summarised the results of the interatomic distances obtained for the ideal and relaxed clean surface in comparison with the results of Barnard *et al.* [3] obtained with a similar DFT-GGA approach. Also in this case the agreement is excellent, within 1.0% for all the distances but the $D_{1,2}\perp$ that turns out to be 0.02Å shorter than that obtained in Ref. [3].

The surface energy for the cleavage surface was calculated according to:

$$\gamma = \frac{E_{sub} - E_{bulk}}{2A} \tag{4.1}$$

where E_{sub} is the total energy of the surface, E_{bulk} represents the total energy of a bulk structure - with the same symmetry - containing as many CdS-pairs as those in the surface, and A is the surface Area. The calculated surface energy turns out to be $\gamma = 0.28 \ \ \mathrm{Jm}^{-2}$, which is identical to that obtained in Ref. [3].

Table 4.1: interatomic distances

CdS	ideal	relaxed	others [3]
$D_{1,2}x$	2.53	2.29	2.29
$D_{1,3}x$	0.84	0.64	0.65
$D_{1,4}x$	3.37	3.50	3.50
$D_{1,2}y$	0.00	0.00	0.00
$D_{1,3}y$	2.09	2.07	2.07
$D_{1,4}y$	2.09	2.06	2.07
$D_{1,2}\perp$	0.00	0.80	0.78
$D_{1,3}\perp$	1.20	1.30	1.31
$D_{1,4}\perp$	1.21	1.55	1.57

The ions S and Cd occupy two inequivalent lattice sites hereafter referred to as *hollow*- and *top*- sites (see Figure 4.2). Two different vacancies were thus taken into account for both cadmium vacancy (V_{Cd}^{top} and V_{Cd}^{hollow}) and sulfur vacancy (V_{S}^{top} and V_{S}^{hollow}). All configurations were described in terms of geometry, electron density of states (DOS) and vacancy formation energy ΔE^{V}.

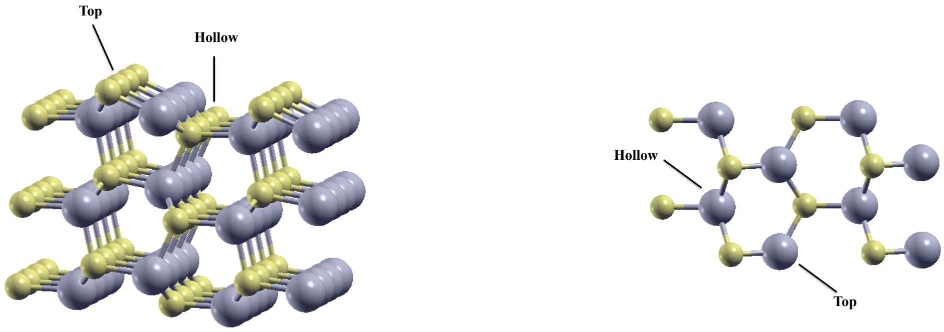

Figure 4.2: Left: partial side-view of the slab model of [10$\bar{1}$0] CdS surface (Cd ions in grey and S ions in yellow); Right: top-view of the surface layer.

4.1.1 Top- and hollow- Cd vacancies in 2x1 surface

Here, we consider a cation vacancy in CdS [10$\bar{1}$0] surface with 2x1 symmetry. In this case while two bottom layers were kept fixed to simulate the infinite bulk, the top three layers were allowed to fully relax. When a cadmium ion was removed either in *top*- or in *hollow*- sites, the sulfur dangling bonds created by the vacancy showed a different behavior. The Cadmium vacancy site in *top* position, is surrounded by three nearest-neighboring S atoms in the surface plane and by one Cd atom in the sub-layer.

The Cd vacancy in *hollow* position is surrounded by four nearest-neighboring S atoms. For both positions the next-nearest neighbors are Cd atoms in the surface plane. The size of the 2x1 surface does not allow to consider them as significative. In Figure 4.3 (left panel) the ideal (a) and final (b) top layer configurations before and after the surface relaxation for a cadmium vacancy in top-site, V_{Cd}^{top}, are depicted. Upon the relaxation around the defect, the nearest-neighboring S atoms moved toward the vacancy site, one S by -0.28% and two S atoms displaced also toward the defect by -0.04%, of the bulk Cd-S bond length (d_0). They are marked in red in Figure 4.3.
As for V_{Cd}^{hollow} (left panel of Figure 4.4) a general expansion of the lattice around the vacancy site is remarkable. The lattice appears distorted. The three S ions moved by +0.06%, +0.39% and +0.43% of d_0, respectively and, in addition, one S ion lying in the adjacent second layer (green color) moved upward, along the direction perpendicular to the surface, toward the vacancy site by -0.06%. As a result, a new S_2 dimer (see Figure 4.4-b) was formed, with S-S bond length of 2.15Å that is larger than the typical sulfur dimer length of 1.89Å .

A similar mechanism was observed by Varghese et al.[42] in Cd-vacancy in CdS nanotubes where they calculated a bond-length as large as 2.12Å, in a sulfur dimer formed on the nanotube surface in the presence of a cadmium vacancy. The minus sign indicates henceforth a contraction of bond-lengths as opposite to an expansion indicated with a positive sign. All the relevant distances from surrounding ions to the defect site are summarized in Table 4.2.

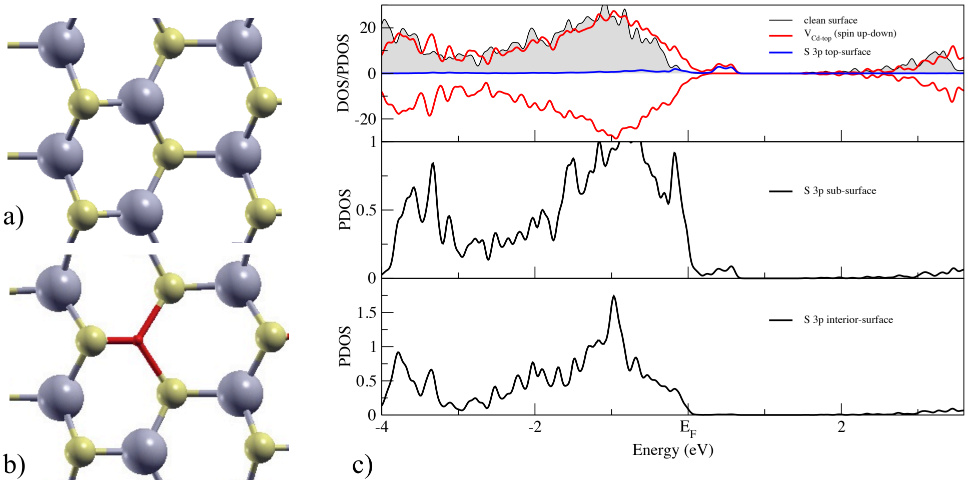

Figure 4.3: V_{Cd}^{top}- Left: Top-view of unrelaxed (a) and relaxed (b) geometry of the CdS [10$\bar{1}$0] defective surface. The vacancy surrounding bonds are shown in red. Right: Calculated total DOS and projected DOS of S-3p dangling bonds (c) (see text for explanation).

Table 4.2: Distances between the vacancy surrounding S atoms and the defects site before and after the relaxation.

defects	ideal (Å)	relaxed (Å)
d(V_{Cd}^{top} - S_{NN})	2.51, 2.51, 2.42	2.39, 2.40, 1.75
d(V_{Cd}^{hollow} - S_{NN})	2.53, 2.53, 2.59, 2.63	3.62, 2.69, 3.62, 2.46

Electron density of states for CdS defective surface remarkably revealed the presence of Cd vacancy in top position. In Figures 4.3-c) the total density of states (DOS) of the defect-free surface (shaded area) is compared to the DOS calculated for the defective system together with the separate contributions (PDOS) of individual orbitals belonging to atoms close to the vacancy site. The Fermi Energy E_F is here considered as the reference level, set to the highest occupied state, i.e. the top of the valence band.

In particular, regarding the V_{Cd}^{top}, the DOS revealed the presence of a peak in the gap as shown in the top-panel of Figure 4.3-c). From the analysis of the electron bands at Γ it turned out that the peak represents an empty state, thus an acceptor level, located close to the valence band maximum. Also, the spin up and down asymmetry, highlighted in red line up and down, indicates different spin contributions: the peak appears in only the spin-up component.

We underline this is an acceptor level located between the valence band-maximum and the mid-value of E_g.

The calculated surface energy gap E_g resulted as large as 1.21 eV. It is smaller, as expected, from DFT-GGA approximation. Considering as 2.42 eV the experimental value of the gap we can deduce that the energy of the peak broadly falls in the range between 1.21-2.42 eV, corresponding to a range in the emission spectrum of 1024-512 nm. Anyhow, the theoretical correction of the band edges will be next discussed in some details. The location of this acceptor level, acting as a trap, makes in turn the vacancy site more reactive. Its role and the eventual shift of its position in the gap due to the interaction between the surface and external agents will be discussed in the next Chapter.

Tang et al. [123] found a similar mechanism in zincblende CdS surface with a Cd vacancy. They ascribed this spin-asymmetry to a magnetic behavior coming from surface effects like low coordination which results in unpaired electrons in S $3p$-orbitals.

In order to understand which orbitals are responsible for the aforementioned acceptor level, the individual contributions of sulfur p-orbitals in different positions of the lattice were also calculated.

The blue line in the top-panel of Figure 4.3-c) is the contribution of the surface S $3p$-orbital. In the central and bottom panel the equivalent orbitals for the sulfur in the sub-surface and in the inner layers, respectively, are plotted for comparison. S $3s$-orbitals did not give any remarkable contributions in the top-valence region. Notice, there is a component in the $3p$ state coming from the sulfur atom below the vacancy site while there are no peaks in the gap region shown in the bottom curve.
In other words, the PDOS supported the fact that, the S $3p$ dangling bonds of S_{NN} are mainly responsible for the new states in the band gap and the distribution of spin density around the Cd vacancy indicates that the main contribution to the total magnetic moment arises from the $3p$ orbitals of S_{NN}, while the magnetic moments on Cd atoms are almost negligible. Also, the S atoms at inner layers (central and bottom panel) gave indeed no contribution. The calculated total magnetic moment for V_{Cd}^{top}, turns out to be 1.32 μ_B
This fact predicts unambiguously that V_{Cd}^{top} creates a new acceptor level in the gap due to $3p$ dangling bonds belonging to S atoms vacancy nearest neighbors.

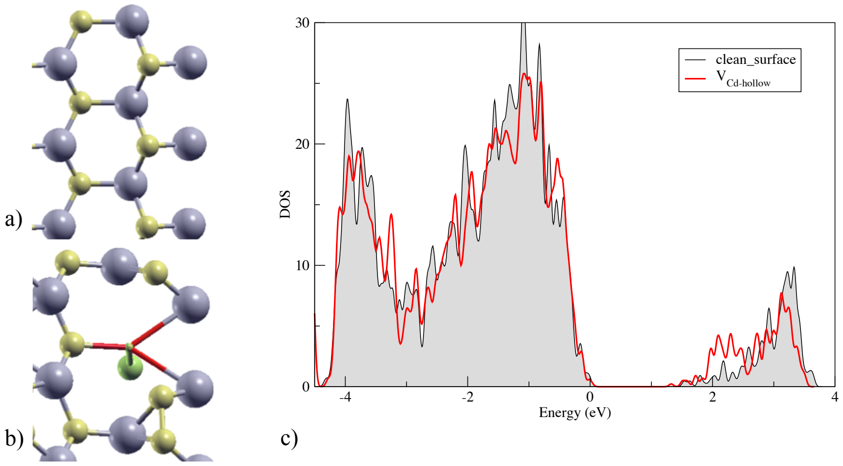

Figure 4.4: V_{Cd}^{hollow}-Left: Top-view of unrelaxed (a) and relaxed (b) geometry of the CdS {10.0} defective surface. The vacancy surrounding bonds are shown in red. S atom in the sub-layer in green. Right: Calculated total DOS for clean and defective surface (c).

The same calculations were performed for the system V_{Cd}^{hollow} and the results are plotted in Figure 4.4-c), where the Cd vacancy at the surface did not lead to significant features in the electronic structure at least close to the band edges. No spin asymmetry was remarked in this case. For the configurations above mentioned, the vacancy formation energy was calculated according to Eq. 3.1 in both S-rich and Cd-rich growth conditions. Results are listed in Table 4.3. The results, reveals in both S-rich and Cd-rich environment of CdS, the cadmium vacancies in hollow position show the

Table 4.3: Vacancy formation energies ΔE^V(eV) in S-rich and Cd-rich conditions.

ΔE^V	S-rich	Cd-rich
V_{Cd}^{top}	1.62	3.36
V_{Cd}^{hollow}	0.52	2.28

lowest formation energy.

In order to have a better understanding of the acceptor level appearing in the band gap, in the system containing V_{Cd}^{top}, we performed a series of calculations to obtain a correct value for the band edges, VBM and CBM, respectively. The procedure is illustrated in the Section 2.5. The reference potential the electron states are referred to, was evaluated as the electrostatic potential in the vacuum region of periodic surface slabs. An example is given in Fig. 4.5 for the system V_{Cd}^{top}. The value of $E_g^{GW} = 2.38$ eV was obtained from bulk calculations. According to the Eqns. (2.39) and (2.40) the band edges resulted E_{BGC} = -5.51 eV, E_{VBM} = -6.70 eV and E_{CBM} = -4.32 eV, respectively. Consequently, the gap opens symmetrically about E_{BGC} as shown in Fig. 4.6. While the VBM is directly related to the work-function, in the GGA all the eigenvalues within the gap are underestimated because of the underestimation of the conduction states. To correct a defect level by shifting it upwards, one may assume the shift to be proportional to the contribution of the conduction states to

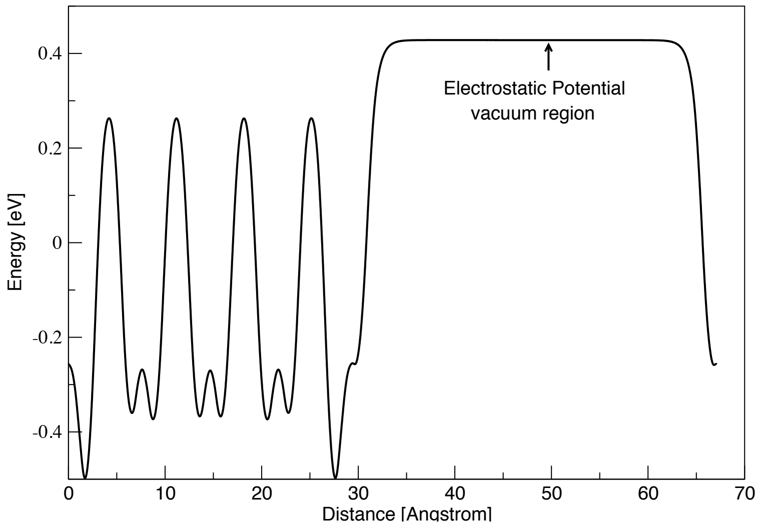

Figure 4.5: Electrostatic potential averaged over planes parallel to the surface calculated for CdS surface. The region to the right around 50Å is the vacuum region, where the energy is set to zero (the vacuum level). The energy decreases at the far right where the next periodic image of the CdS slab begins.

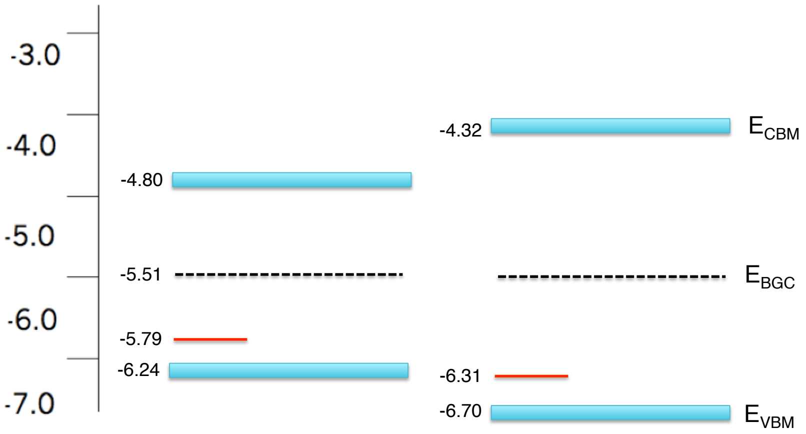

Figure 4.6: V_{Cd}^{top}. -Left: Band edge positions for the CdS surface within DFT, E_g^{DFT}. Right: band gap after addition of GW corrections, E_g^{GW} denotes the band gap center.

the defect level. This contribution in turn may be assumed to be proportional to the energy of the level relative to the conduction bands, i.e., the corrected defect energy $\epsilon_{defect}^{corrected}$ is rescaled by the correction of the band gap, and is given by $\epsilon_{defect}^{corrected} = \epsilon_{defect}^{GGA}(E_{gap}^{GW}/E_{gap}^{GGA})$. Thus the levels close to the top of the valence band are almost non-shifted while the levels close to the conduction band are shifted about E_{gap}. This approach is empirical. A fully theoretical description of the levels inside the gap, by means of time dependent DFT or full GW calculations on defective surfaces, is mandatory in the follow-up of this work. Anyhow, with such empirical correction $\epsilon_{defect}^{corrected}$ = -6.31 eV which corresponds to an emission band of :

$$\Delta(E_{CBM} - \epsilon_{defect}^{corrected}) = 1.98 \text{ eV} \equiv 626 \text{ nm (orange-red)}$$

Another study [127], carried out on cadmium pigments (CdS and CdS_xSe_{1-x}), showed two luminescence bands at around 640 and 820 nm, respectively, ascribed to trap emissions. In order to rule out any effects due to the size of the simulation cell, calculations on a larger surface model will be discussed in the following.

4.1.2 Top- and hollow- S vacancies in 2x1 surface

In analogy with the results described previously for Cd vacancies, also the presence of S vacancy both in V_S^{top} and V_S^{hollow} created dangling bonds in the surface Cd atoms nearest neighbors to the vacancy. In V_S^{top}, as plotted in Figure 4.7-b) compared to the initial clean surface in Figure 4.7-a), the three Cd atoms surrounding the S vacancy move in-plane toward the vacancy site and create two new Cd-Cd bonds of 2.52Å and 2.53Å, respectively. The relaxed distance between the nearest Cd ion and the vacancy site is now decreased by about -0.25% with respect to the initial one (2.42Å).

Also in V_S^{hollow} (see Figure 4.8-b), three nearest neighborings Cd atoms move toward

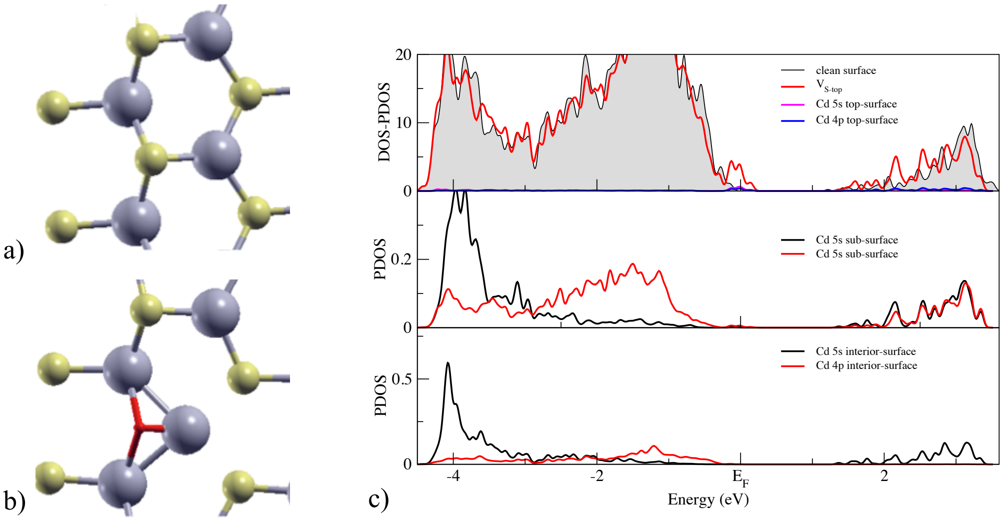

Figure 4.7: V_S^{top} -Left: Top-view of unrelaxed (a) and relaxed (b) geometry of the CdS $[10\bar{1}0]$ defective surface. The vacancy surrounding bonds are shown in red. Right: Calculated total DOS and projected DOS of Cd dangling bonds (c) (see text for explanation).

the vacancy site by -0,2%, -0,16%, and -0.15%. In addition, Cd atom from underlying layer (green color) shortens the distance by -0,14%. All the relevant distances from surrounding ions to the defect site are summarized in Table 4.4. With the same

Table 4.4: Distances between the vacancy surrounding Cd atoms and the defects site before and after the relaxation.

defects	initial (Å)	relaxed (Å)
d(V_S^{top} - S_{NN})	2.53, 2.53, 2.42	2.53, 2.54, 1.82
d(V_S^{hollow} - S_{NN})	2.59, 2.51, 2.51, 2.59	2.54, 2.08, 2.12, 2.21

procedure adopted for Cd-vacancies we calculated the total and partial DOS for both V_S^{top} and V_S^{hollow}. Results are reported in Figures 4.7-c) - 4.8-c). As for V_S^{top}, in the top panel of Figure 4.7-c) the red line represents the total DOS for S vacancy while magenta and blue curves are the individual 5*s* and 4*p* orbitals contributions to the density of states coming from the nearest Cd atoms in the top-surface layer. Also in this case no spin asymmetry was remarked. For comparison, the partial contribution of the same orbitals coming from Cd atoms located in sub- and inner- layers are also given in the central and bottom panel, respectively. Total and partial DOS show that Cd 5*s* and 4*p* are responsible for new states in the region located in proximity of the valence band maximum. As opposite to what found for V_{Cd}^{top} where the new peak is

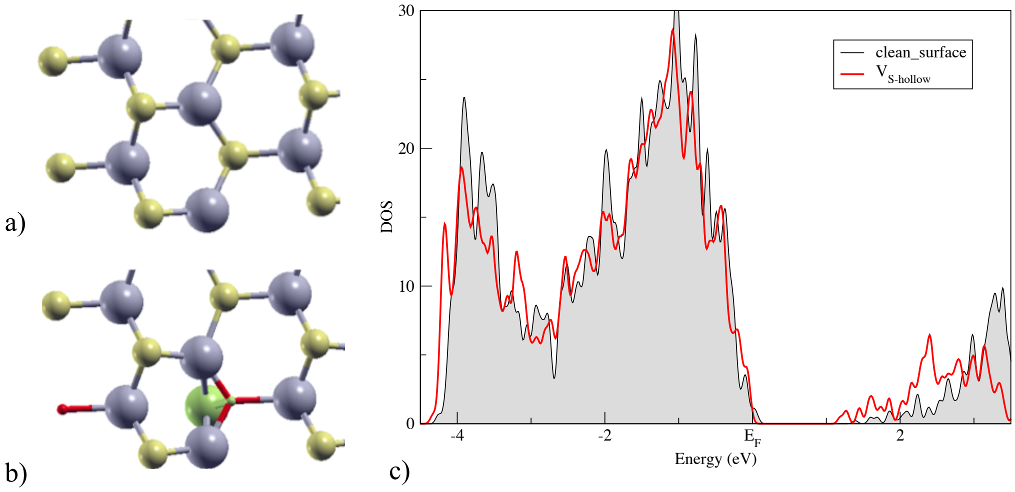

Figure 4.8: V$_S^{hollow}$-Left: Top-view of unrelaxed (a) and relaxed (b) geometry of the CdS {10.0} defective surface. The vacancy surrounding bonds are shown in red. Cd atom in the sub-layer in green. Right: Calculated total DOS for clean and defective surface (c).

clearly located above the Fermi energy, the new peak in V$_S^{top}$ crosses the Fermi energy indicating mostly a rearrangement of occupied electron states in this region. Further investigation considering larger simulation cells and a proper treatment of the band gap is needed to shed light on this point. Regarding the V$_S^{hollow}$ the electronic structure compared to clean surface does not change significantly except for new states close to the bottom of the conduction band minimum that do not significantly affect the band gap. In both S vacancies no asymmetry between spin up and down was found. The vacancy formation energy of S vacancies in both S-rich and Cd-rich growth conditions are listed in Table 4.5. As shown in Cadmium vacancies the formation energy are lowest in V$_S^{top}$ in both conditions.

Table 4.5: Vacancy formation energies ΔE^V(eV) in S-rich and Cd-rich conditions.

ΔE^V	S-rich	Cd-rich
V$_S^{top}$	2.19	0.45
V$_S^{hollow}$	2.91	1.17

4.1.3 Top- and hollow- Cd vacancies in 2x2 surface

In this section, we show the study of same type of vacancies previously accounted for but in larger simulation cells (2x2) containing up to 160 atoms, in order to rule out eventual size effects on the geometrical and electronic structure in the region of the defects. We focused first on Cd vacancies, since they play a key role because of the extra acceptor level in the gap. Following the same procedure adopted in section 4.1.2 we calculated relaxed distances and energy bands for Cd vacancy in both *top* and *hollow* positions. In this case besides the first shell of vacancy neighbors (NN), also the second one of next nearest neighbors (NNN) will be taken into account. In V_{Cd}^{top}, two nearest neighboring S atoms in the same layer moved symmetrically inward by -26.8% and a third one by -8.7%, while a Cd atom in the layer below ($Cd_{\perp}$) raised toward the vacancy by -2.92%. The relaxation of the Cd_{NNN} atoms is inward the vacancy by -1.92%, -0.03% and -4.28%, respectively. Anyhow, the displacement of atoms is more pronounced in the first shell of neighbors. The corresponding DOS, in figure 4.9 -c), reveals a well defined peak in the band gap due to a residual of the spin-down contribution. The Projected-DOS (central panel) confirms that this defect state is due to the $3p$-states of S_{NN} (dangling bonds) lying in-plane, while no contribution is detected from S atoms of layers below. Any contributions from $Cd_{\perp}$ is also negligible. According to the same procedure adopted for smaller simulation cells, band edges and band gap center were obtained from Eqns. (2.39) and (2.40). The calculated values (see Fig. 4.10) were E_{BCG} = -5.21 eV, E_{VBM} = -6.39 eV and E_{CBM} = -4.02 eV, respectively. The empirical correction to the Kohn-Sham eigenvalue corresponding to the defect level, $\epsilon_{defect}^{corrected} = \epsilon_{defect}^{GGA}(E_{gap}^{GW}/E_{gap}^{GGA})$, leads to a preliminary value for the deep trap $\epsilon_{defect}^{corrected}$ = -5.28 eV which is associated to an emission band in the

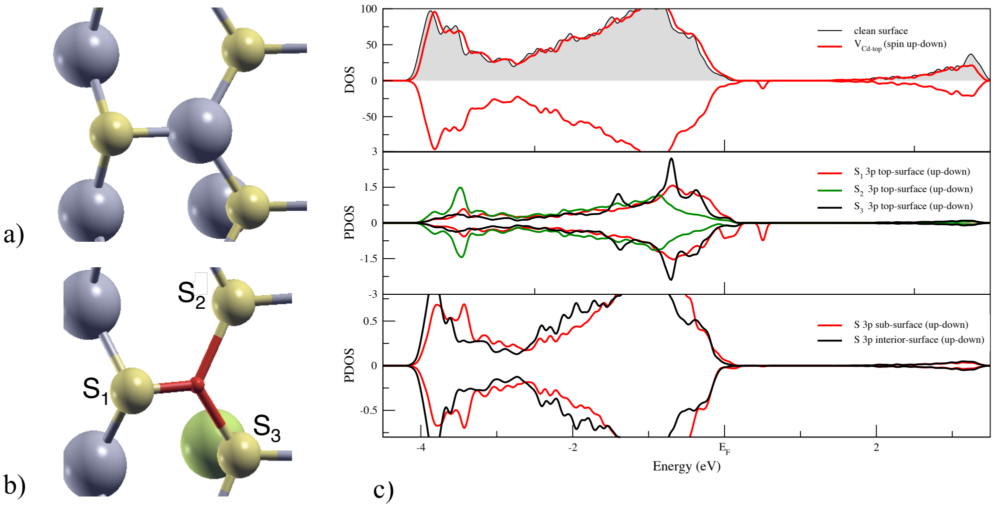

Figure 4.9: V_{Cd}^{top}-Left: Top-view of unrelaxed (a) and relaxed (b) geometry of the CdS {10.0} defective surface. The vacancy surrounding bonds are shown in red. Right: Calculated total DOS and projected DOS of S-3p dangling bonds (c) (see text for explanation).

near-infrared:

$$\Delta(E_{CBM} - \epsilon_{defect}^{corrected}) = 1.26 \text{ eV} \equiv 984 \text{ nm (near-infrared)}$$

Among the several studies carried out in cadmium pigments related to emission in the red and near-infrared regions associated with trap states, our result falls in the experimental range (see Ref. [39]) where the emission band occurs above 950 nm. Rosi et al. [128] reported, in commercial pigments of 100% pure hexagonal CdS, two distinct peaks at 1.64 eV (757 nm) and 1.24 eV (998 nm). In pure hexagonal CdS reference samples used for comparison, they interestingly found only a single peak at 1.57 eV (791 nm). This result indicated that crystalline composition is not the only factor affecting fluorescence properties but the location of defects (bulk vs surface), the concentration, and the defect structure itself play a relevant role. Our results support the fact that the same cation vacancy in various positions in the hexagonal structure, namely in the bulk, in *top* and *hollow* lattice sites, yields to different rearrangements of the band structure.

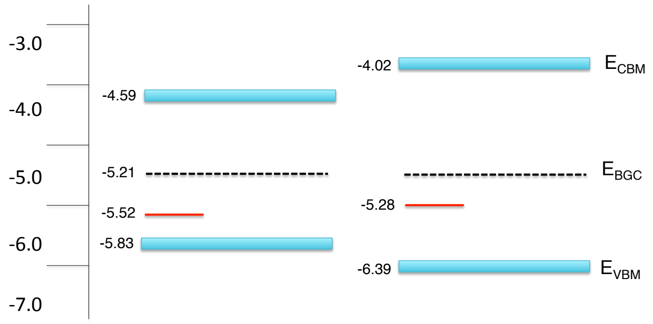

Figure 4.10: V_{Cd}^{top} - Left: Band edge positions for the CdS surface within DFT, E_g^{DFT}. Right: band gap after addition of GW corrections, E_g^{GW} denotes the band gap center

As for V_{Cd}^{hollow}, the geometry of the surface in the presence of the defect does appear remarkably affected. Indeed, two of three S_{NN} in the plane moved outward by +17.39% and one displaced inward by -14.29%. The $Cd_{\perp}$ atom moved toward the vacancy by -15.92% (green color). The relaxation of the next nearest neighbors Cd atoms is outward the vacancy by +0.72%, +0.83% and inward by +4.28% as shown in 4.11-b). As opposite to what observed in the smaller simulation cell (see Fig. -b) no S_2 dimer was formed in this case, indicating that next nearest neighbors have a role in the lattice relaxation around the defect. In Fig. 4.11-c) the DOS shows that the defective surface changes with respect to the clean one (shaded area): vacancy-DOS (red curve) follows different spin up and down profiles.

A double shallow peak appears in the spin down part of the density of states that

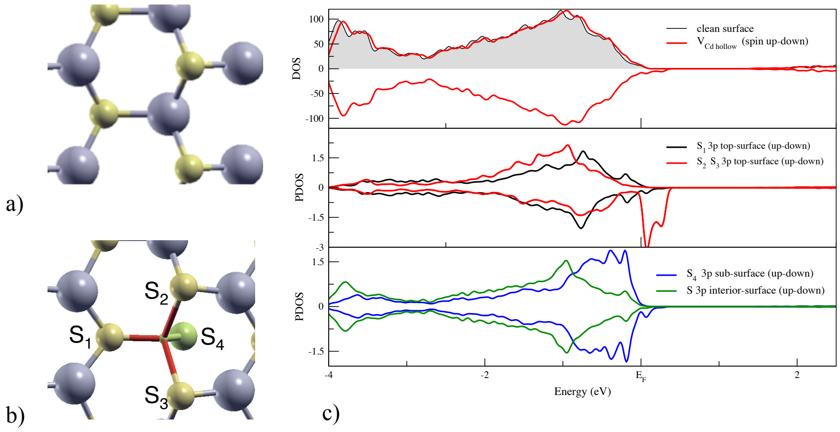

Figure 4.11: V_{Cd}^{hollow}-Left: Top-view of unrelaxed (a) and relaxed (b) geometry of the CdS {10.0} defective surface. The vacancy surrounding bonds are shown in red. Right: Calculated total DOS and projected DOS of S-3p dangling bonds (c) (see text for explanation).

includes $3p$-states of sulfur atoms laying both in-plane and in the layer below (blu curve, bottom panel). The calculated values (see Fig. 4.12) were E_{BCG} = -5.25 eV, E_{VBM} = -6.44 eV and E_{CBM} = -4.05 eV, respectively. With such empirical correction, the values for the deep traps were $\epsilon_{defect}^{corrected}$ = - 5.48 eV and $\epsilon_{defect}^{corrected}$ = -5.59 eV which are associated to two emission bands in the near-infrared:

$$\Delta(E_{CBM} - \epsilon_{defect}^{corrected}) = 1.43 \text{ eV} \equiv 867 \text{ nm (near-infrared)}$$

$$\Delta(E_{CBM} - \epsilon_{defect}^{corrected}) = 1.54 \text{ eV} \equiv 805 \text{ nm (near-infrared)}$$

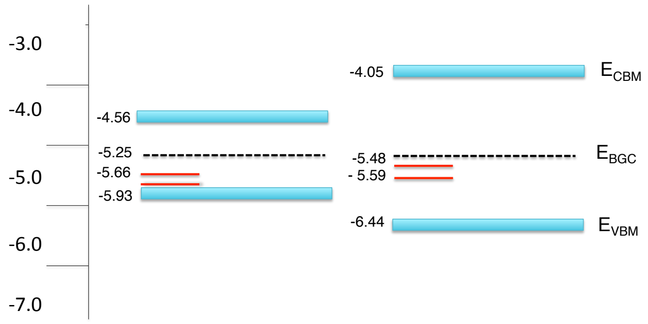

Figure 4.12: V_{Cd}^{hollow} - Left: Band edge positions for the CdS surface within DFT, E_g^{DFT}. Right: band gap after addition of GW corrections, E_g^{GW} denotes the band gap center

Table 4.6 summarizes the results of the distances before and after structural optimization for V_{Cd}^{top} and V_{Cd}^{hollow}. For the configurations above mentioned, the vacancy formation energy was calculated according to Equation 3.1 in both S-rich and Cd-rich

Table 4.6: Distances between the vacancy surrounding S_{NN} atoms and Cd_{NNN} atoms before and after the relaxation. In parentheses are the number of elements involved in the defect. All the distances are calculated in the layer containing the defect except for elements marked with $_\perp$ indicating ions in the sub-layer.

defects	ideal (Å)	relaxed (Å)
d(V_{Cd}^{top} - S_{NN})	(2S) 2.51, (S) 2.42, ($S_\perp$) 3.84	(2S) 2.29 (S) 1.77 ($S_\perp$) 3.72
d(V_{Cd}^{top} - Cd_{NNN})	(2Cd) 4.14 (2Cd) 3.62 (2Cd) 4.33	(2Cd) 4.06 (2Cd) 3.49 (2Cd) 4.15
d(V_{Cd}^{hollow} - S_{NN})	(2S) 2.53 (S) 2.59 ($Cd_\perp$) 2.63	(2S) 2.97 (S) 2.22 ($Cd_\perp$) 2.21
d(V_{Cd}^{hollow} - Cd_{NNN})	(2Cd) 4.14 (2Cd) 4.33 (2Cd) 3.61	(2Cd) 4.17 (2Cd) 4.19 (2Cd) 3.64

growth conditions. Results are listed in Table 4.7. Formation energies indicate that, at thermal equilibrium, the concentration of defects in top position is higher than that in hollow: at any temperature, the presence of V_{Cd}^{top}, both in S-rich and Cd-rich conditions results favorite with respect to V_{Cd}^{hollow}.

Table 4.7: Vacancy formation energies ΔE^V(eV) in S-rich and Cd-rich conditions.

ΔE^V	S-rich	Cd-rich
V_{Cd}^{top}	1.56	3.31
V_{Cd}^{hollow}	2.12	3.87

4.1.4 Top- and hollow- S vacancies in 2x2 surface

The formation of a S vacancy creates three dangling bonds from nearest neighboring Cd atoms when V_S is in *top* position and four when it is in *hollow* position while the next nearest neighbors are all S atoms in the surface plane. In V_S^{top} the three Cd_{NN} move in-plane toward the vacancy site by -4.6% (two of them) and -20.1% as shown as plotted in Figure 4.13-b) compared to the initial clean surface in Figure 4.13-a). The relaxed distance between the two Cd_{NN} closest to the vacancy remarkably decreased by about 57.6% with respect to the initial one (6.82Å). Also the next nearest neighbors S atoms move inward the vacancy by -3.50%, -2.28% and -4.12%. In V_S^{hollow} (see Figure 4.14-b), two nearest neighboring Cd atoms displaced in-plane toward the

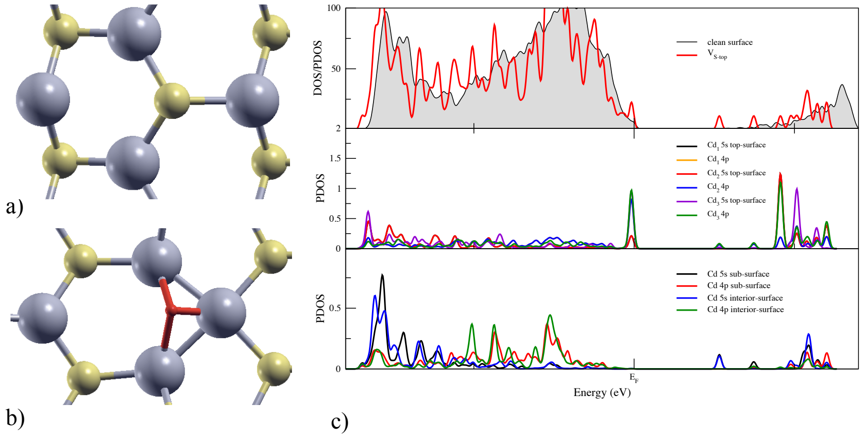

Figure 4.13: V_S^{top}-Left: Top-view of unrelaxed (a) and relaxed (b) geometry of the CdS {10.0} defective surface. The vacancy surrounding bonds are shown in red. Right: Calculated total DOS and projected DOS of Cd dangling bonds (c) (see text for explanation).

vacancy site by 24.16% and their distance decreased of 25.5%, while the other Cd atom in the same plane moved away by 3.53%. The next nearest neighbors relaxed inward the defect by -4.33%, -6.12% and -2.86%. In addition, Cd atom from sub-layer (green color) shortens the distance by -9.20%. All the relevant distances between surrounding ions and the defect site are summarized in Table 4.8. In parentheses are the number and the elements involved. As for V_S^{top}, (see Figure 4.13-c) in the top panel the red line represents the total DOS for S vacancy while in the center panel the individual 5s and 4p orbitals contributions to the density of states coming from the Cd_{NN} atoms in the top layer. No spin asymmetry was remarked. For comparison, the partial contributions of the same orbitals coming from Cd atoms located in sub- and inner- layers are also given in the bottom panel. Total and projected DOS reveal

Table 4.8: Distances between the vacancy surrounding Cd_{NN} atoms and $S_N NN$ atoms before and after the relaxation. In parentheses are the number and the atoms involved

defects	initial (Å)	relaxed (Å)
d(V_S^{top} - Cd_{NN})	(2Cd) 2.52	(2Cd) 2.41
	(Cd) 2.42	(Cd) 1.93
d(V_S^{top} - S_{NNN})	(2S) 4.14, (2S) 4.14	(2S) 3.99, (2S) 4.04
	(2S) 4.34	(2S) 4.16
d(V_S^{hollow} - Cd_{NN})	(2Cd) 2.50, (Cd) 2.60	(2Cd) 1.90, (Cd) 2.67
	(Cd) 2.59	(Cd) 2.35
d(V_S^{hollow} - S_{NNN})	(2S) 4.14, (2S) 4.14	(2S) 3.96, (2S) 4.08
	(2S) 4.34	(2S) 4.02

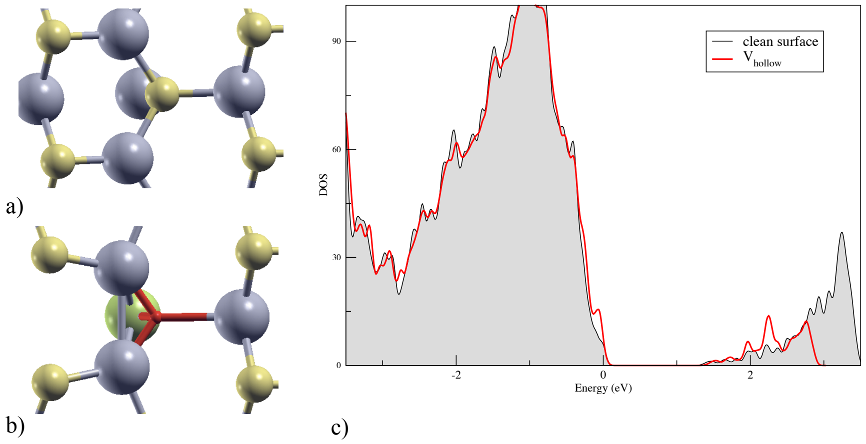

Figure 4.14: V_S^{hollow}-Left: Top-view of unrelaxed (a) and relaxed (b) geometry of the CdS {10.0} defective surface. The vacancy surrounding bonds are shown in red. Cd atom in the sub-layer in green. Right: Calculated total DOS for clean and defective surface (c).

that Cd 5s and 4p are responsible for a peak in the valence band and other peaks close to the conduction band edge. The first peak indicates mostly a rearrangement of occupied electron states in this region, while the second ones are likely related to a shallow defect level. Several experimental studies reported sulfur vacancies energy levels at about 0.7 eV below the conduction band in CdS [129, 130, 131].

In Figure 4.14-c), the DOS of V_S^{hollow} shows that the surface does not change significantly the electronic structure the trend is similar of clean surface. Also in this vacancy no asymmetry between spin up and down was found. In both surfaces containing V_S^{top} and V_S^{hollow}, the arrangement around the defect is different compared to the initial configuration.

For the structure previously described, the vacancy formation energy was calculated according to Equation 3.1 in both S-rich and Cd-rich growth conditions. Results are listed in Table 4.9. The relatively lower formation energy of Cd vacancies (compared to that of S vacancies) on the surface studied has been previously reconciled with often-reported sulfur deficiency by demonstrating that most of the experimental observations were conducted on samples prepared in environments that were Cd-rich.

Table 4.9: Vacancy formation energies ΔE^V (eV) in S-rich and Cd-rich conditions.

ΔE^V	S-rich	Cd-rich
V_S^{top}	2.14	0.39
V_S^{hollow}	2.75	1.00

CHAPTER 5

Adsorption of O_2 and H_2O on clean and defective $[10\bar{1}0]$ CdS surface

In this Chapter we describe a simplified model of the combined effects of exposure to air and humidity of clean and defective CdS $[10\bar{1}0]$ surface. To this end, the CdS $[10\bar{1}0]$ surface was allowed to interact either with isolated oxygen or water molecules, and then with a combination of them.

For each interaction we studied the geometrical and electronic structure and calculated the adsorption energy (E_{ad}) in the following way:

$$E_{ad} = E_{sub+mol} - [E_{sub} + nE_{mol}]$$

where $E_{sub+mol}$ is the total energy of the combined system containing the surface and n molecules, E_{sub} is the total energy of the clean surface, and E_{mol} is the energy of a single isolated molecule.

The bonding charge analysis, that gives an estimate of the electron charge transfer, was evaluated according to:

$$\Delta\rho(\mathbf{r}) = \rho_{sub+mol} - \rho_{sub} - \rho_{mol}$$

where $\rho_{sub+mol}(\mathbf{r})$, $\rho_{sub}(\mathbf{r})$ and $\rho_{mol}(\mathbf{r})$ are the charge densities of the whole system, the isolated substrate and the adsorbate, respectively.

5.1 O_2 and H_2O @ clean $[10\bar{1}0]$

The interface between a surface and a vapor or liquid governs the interaction between the two phases, and influences the behavior of the surface in many important ways. In order to understand, at atomic level, the oxidation and hydration mechanisms related to degradation process in CdS pigment, we present the early stages of the interaction between the hexagonal clean and defective $[10\bar{1}0]$ surface of CdS and O_2 and H_2O molecules to simulate the combined effects of exposure to air and humidity.

In both clean and defective $[10\bar{1}0]$ surfaces the molecules were placed on top of the relaxed surface layer in several arbitrary initial positions. The molecules and the three outermost atomic layers of the surface were then allowed to relax until the interatomic forces vanished. This condition was reached with a threshold on forces as strict as $\leq 10^{-3}$eV/Å. The two bottom layers were kept fixed to the bulk positions to simulate the infinite crystal. Due to the presence of molecules, the dispersion corrected DFT (DFT-D2) approach proposed by Grimme [132] and implemented by Barone and co-workers [133] was used to account for the van der Waals (vdW) dispersion forces in the calculations. To this end, lattice parameters were re-calculated to take into account the dispersion correction. They were $a_0 = 4.20$Å and $c/a = 1.63$.

O_2 @ clean CdS - Four setups were considered as initial conditions, where the molecules were initially positioned at a distance as large as about 2Å above the Cd and S sites in both the two non-equivalent positions *top* and *hollow*, respectively. The final relaxed configurations corresponding to the lowest energy dispositions are shown in Fig. 5.1. The calculated adsorption energies suggest the favorite sites that resulted as *top* on Cd and *hollow* on S with the adsorption energies $E_{ad}^{top@Cd}$ = -13.06 kJmol^{-1} and $E_{ad}^{hollow@S}$ = -13.54 kJmol^{-1}, respectively, manifesting the molecule to be physisorbed. In Figure 5.2 is reported the lowest energy relaxed configuration with O_2 located on top of Cd site (left) and the corresponding bonding charge. In this case both the intra- and interlayer distances did not change remarkably while the O-O bond within the oxygen molecule increases from 1.20Å to 1.23Å. The bonding charge analysis reveals an accumulation of charge in the region between O_2 and the Cd surface ion (red area) indicating a rearrangement of electron charge around the O_2 molecule.

H_2O @ clean CdS - The oxygen molecule was then replaced by a water molecule, the result is shown in Fig. 5.3. The H_2O moved toward the *hollow* Cd. The adsorption energy, $E_{ad} = -32.09$ kJmol^{-1}, is higher than that obtained for O_2 and yet, the mechanism suggested is again a physisorption. Also in this system, no evident displacements of the atoms in the substrate are detected. The change of the angle within the water molecule is, conversely, noticeable. It appears to decrease from 104.39° to

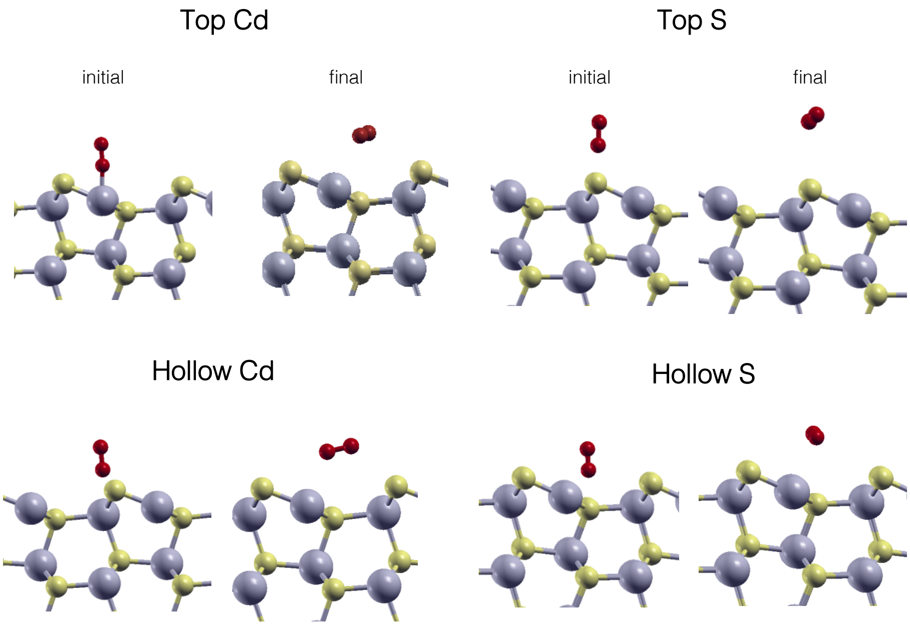

Figure 5.1: Initial and final configuration of interaction between O_2 and CdS [10$\bar{1}$0] surface in Cd- and S- top/hollow positions.

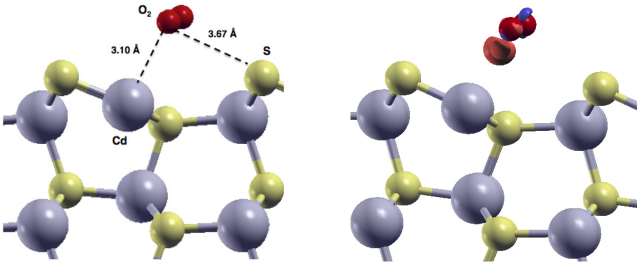

Figure 5.2: Interaction between the CdS [10$\bar{1}$0] surface and an isolated O_2 molecule: relevant inter-atomic distances (left) and bonding charge analysis (right)

103.25°, close within 1%, to the experimental value 104.5° [134].
Concerning the bonding charge analysis, the water dipole was evident and a slight accumulation (red area) of charge between oxygen and the surface *hollow* Cd resulted in opposition to a depletion of charge (blu area) in the hydrogen regions.

O_2 + H_2O @ clean CdS - Finally, a combination of O_2 and H_2O was considered. The two molecules were placed on the surface free to relax with no constraints. The final configuration is reported in Figure 5.4. The O_2 molecule holds the favorite adsorption site above the *top* Cd while H_2O is located on top of the *hollow* S and is oriented parallel to the surface with the oxygen atom closer to O_2. Again, no atomic position changed within the substrate. The angle $H\hat{O}H$ decreases from 104.39° to 103.25°. A re-arrangement of the charge results in an accumulation in the region

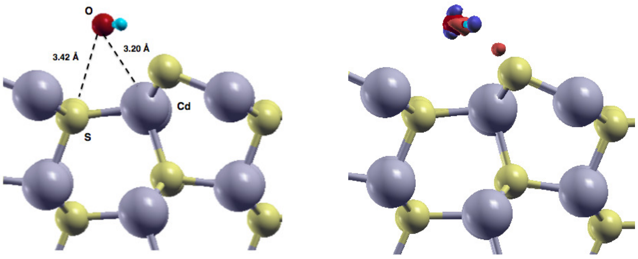

Figure 5.3: Interaction between the CdS {10.0} surface and an isolated H_2O molecule: relevant interatomic distances (left) and bonding charge analysis (right)

between H_2O and S and partially between O_2 and Cd. The adsorption energy of this system, $E_{ads} = -46.40\ \mathrm{kJmol}^{-1}$, indicates a physisorption.

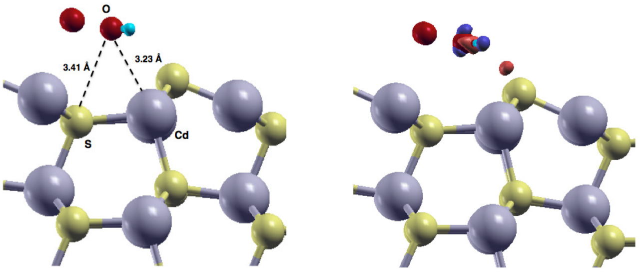

Figure 5.4: Interaction between the CdS {10.0} surface and O_2 + H_2O molecules: relevant interatomic distances (left) and bonding charge analysis (right)

The electronic and geometrical analysis demonstrate that, the physical adsorption of the aforementioned molecules on the cleavage surface turns out to be the dominant mechanism. In other words, the clean surface is predicted to be unreactive to the interaction with air and humidity.

The following section we will consider the same interaction with the defective surface with a particular focus on the V_{Cd}^{top} and V_{S}^{hollow} vacancies, i.e. those sites corresponding to the highest adsorption energy.

5.2 O_2 and H_2O @ defective $[10\bar{1}0]$

In this section we illustrate the interaction between V_{Cd}^{top} and V_{S}^{hollow} in the CdS $[10\bar{1}0]$ and the molecules O_2 and H_2O. The overall procedure is the same adopted for the interaction between molecules and clean surface. The molecules were placed at a distance of about 2Å on top of the vacancy site.

O_2 @ V_{Cd}^{top} - In Figure 5.5-a) the relaxed configuration of O_2 located above the V_{Cd}^{top}, is shown. The geometry of defective surface in the proximity of the vacancy site changed remarkably. The oxygen molecule adsorbed on the S atom nearest the vacancy creating a bond S-O_2 of 1.75Å. The same S atom, in turn, emerged from the surface and its bond with the Cd ion stretched from 2.55Å to 2.73Å. The O-O bond within the oxygen molecule increases from 1.23Å to 1.32Å. This position corresponds to an adsorption energy as large as -62.38 kJmol^{-1}. The bonding charge analysis revealed an accumulation of charge on O_2 (red area) and a slight depletion region (blue area) on the S ion, as shown 5.5-b). No spontaneous dissociation was observed at this level of theory, but the strong adsorption energy, the weakening of Cd-S bond and the formation of the SO_2 group makes this adsorption a first relevant contribution to the understanding of the more complex oxidation reactions:

$$CdS + 2O_2 \longrightarrow Cd^{2+} + SO_4^{2-} \tag{5.1}$$

$$CdS + 2O_2 + H_2O + h\nu \longrightarrow CdSO_4 \cdot H_2O \tag{5.2}$$

that include the intervention of light (photon energy $= h\nu$). In fact, Eq. 5.2 are supposed to yield [26, 22, 17] to the phenomenon of a gradual fading and craquelure of originally bright yellow paint.

The rearrangement of the electron density of the molecule on V_{Cd}^{top} is highlighted in the study of the density of states. The DOS revealed the presence of a peak in the gap, as shown in the top-panel of Figure 5.5-c), very similar to that already found for V_{Cd}^{top}. The Projected DOS (central and bottom panels) showed that this defect state is due to the superposition of 3p-states of S_{NN} atom and 2p-states of oxygen involved in the binding.

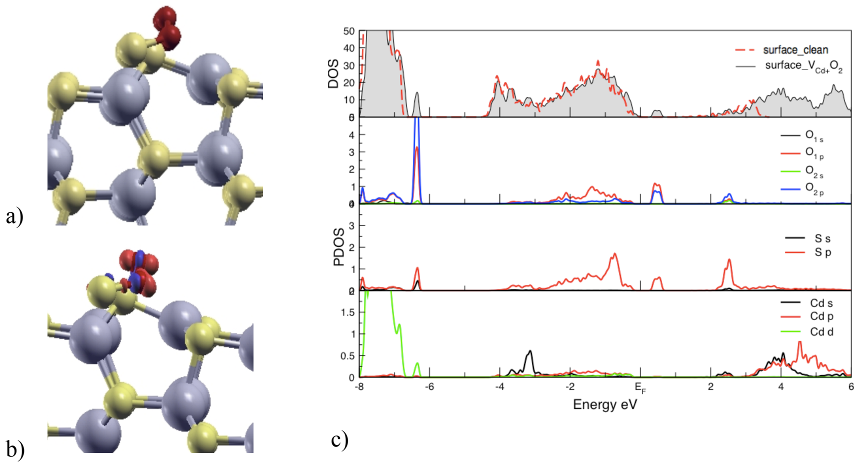

Figure 5.5: Left: side view of relaxed interaction between defective surfaceV_{Cd-top} and O_2(a) bondin-charge of interaction (b) Right: Calculated total DOS and projected DOS of of defective surface and oxygen (c).

The band gap center and the band edges, E_{VBM} and E_{CBM}, were evaluated also in this system (see Fig. 5.6) with the approach described in the Sec. 4.1.2. The peak in

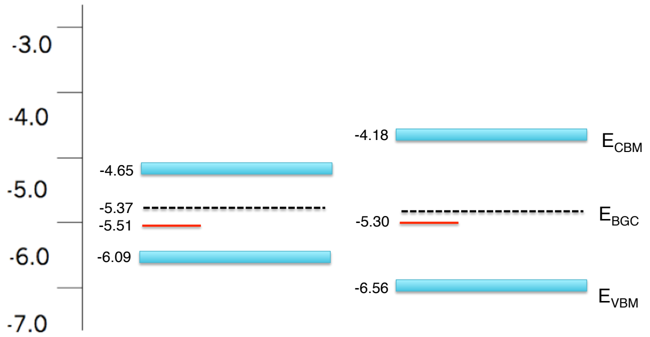

Figure 5.6: O_2 @ V_{Cd}^{top}. Left: Band edge positions within DFT, E_g^{DFT}. Right: band gap after addition of GW corrections. E_{BGC} denotes the band gap center. In red, the defect level.

the gap (-5.30 eV) is associated to an emission band of:

$$\Delta(E_{CBM} - \epsilon_{defect}^{corrected}) = 1.12 \text{ eV} \equiv 1107 \text{ nm (near-infrared)}$$

Further investigation using the nudged elastic band method (NEB) [135] is needed to estimate the energy barrier required for eventual sulfur desorption together with several layers of oxygen molecules to ensure a more realistic model. This result is a part of the debate on the initial photo-oxidation process in which CdS produce CdO, $CdSO_4$ and SO_2 gas. Van der Snickt et al. [22] have observed the formation of $CdSO_4$*$2H_2O$ and $[NH4]_2Cd(SO_4)_2$ on the surface of faded cadmium yellow paints in the works of James Ensor (1860-1949) due to the presence of high relative humidity environments that convert the SO_2 in H_2SO_4, resulting in acid hydrolysis of the paint binding medium.

$\underline{H_2O \text{ @ } V_{Cd}^{top}}$ - The oxygen molecule was then replaced by a water molecule in the same position and then let free to relax. The final configuration in shown in Figure 5.7-a). The water molecule positioned on V_{Cd}^{top} moved toward the Cd_{NN} in top position with a the final distance of 2.50Å , while the distance from the S_{NN} was 4.52Å . On the basis of the bonding charge analysis (see Fig. 5.7-b) a re-arrangement of the electron charge resulted in an accumulation (red area) in the region between H_2O and Cd on top, and a depletion (blue area) of charge on the Cd ion.

Total and projected DOS showed that only *3p* S dangling bonds are responsible for new states in the region located in proximity of the valence band maximum while no contribution from the water is relevant. The adsorption energy, E_{ad} = -62.29 $kJmol^{-1}$, is higher than that obtained for O_2 and the mechanism suggested is again a chemisorption.

The band gap center and the band edges, E_{VBM} and E_{CBM}, were evaluated also in

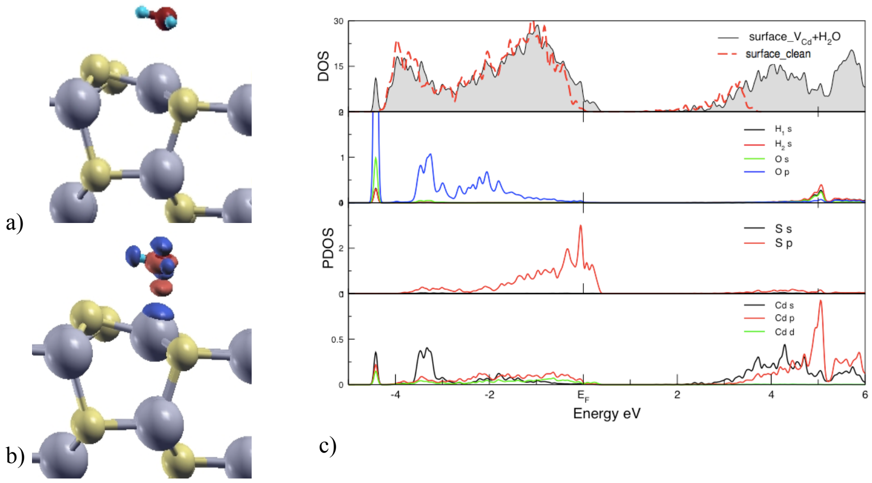

Figure 5.7: Left: side view of relaxed interaction between defective surface V^{top}_{Cd}. and H_2O(a) bonding-charge of interaction (b) Right: Calculated total DOS and projected DOS of defective surface and water (c).

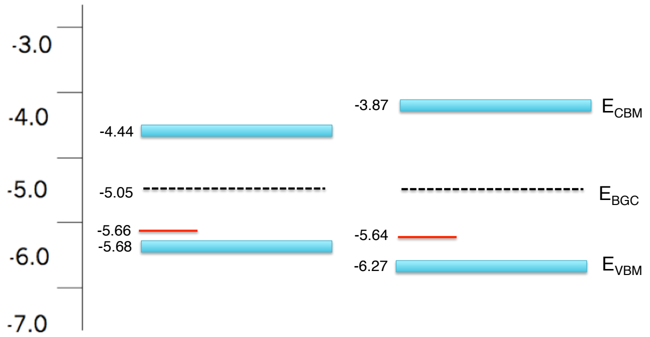

Figure 5.8: H_2O @ V^{top}_{Cd}. Left: Band edge positions within DFT, E_g^{DFT}. Right: band gap after addition of GW corrections. E_{BGC} denotes the band gap center. In red, the defect level.

this system (see Fig. 5.8) with the approach described in the Sec. 4.1.2. The peak in the gap (-5.64 eV) is associated to an emission band of:

$$\Delta(E_{CBM} - \epsilon^{corrected}_{defect}) = 1.78 \text{ eV} \equiv 697 \text{ nm (red)}$$

Also in this case as previously seen in Sec. 4.1.2, the peak falls in the range of red-infrared region. The presence of water shifts the acceptor level toward the VBM. Also in this case, a larger number of water molecules will make the wet model more realistic.

$\underline{O_2 \ @ \ V_S^{hollow}}$ - The same interactions were studied on the surface with S vacancy in hollow position. The molecules of O_2 and H_2O were been located on top the V_S^{hollow}. Regarding the interaction vacancy-O_2 (see Fig. 5.9-a) the molecule fully penetrated in the S vacancy site: it occupied a substitutional position and created the new bonds of 2.16Å , 2.17Å , 2.24Å with three Cd$_{NN}$ atoms in the surface layer and one of 2.22Å with a Cd atom in the layer below. The strong adsorption of O_2 corresponded to a high value of E$_{ad}$ = -77.53 kJmol^{-1}. The geometrical structure was affected also in the adjacent layers due to absorption of the molecule. The bonding-charge in figure 5.9-b) showed the accumulation (red area) of charge in O_2 molecules and a depletion (blue area) in neighboring Cd atoms. The DOS and PDOS in Fig. 5.9 -c) show no extra levels in the gap, but a re-arrangement of the valence region: oxygen p-states are close to the valence band edge below the Fermi level.

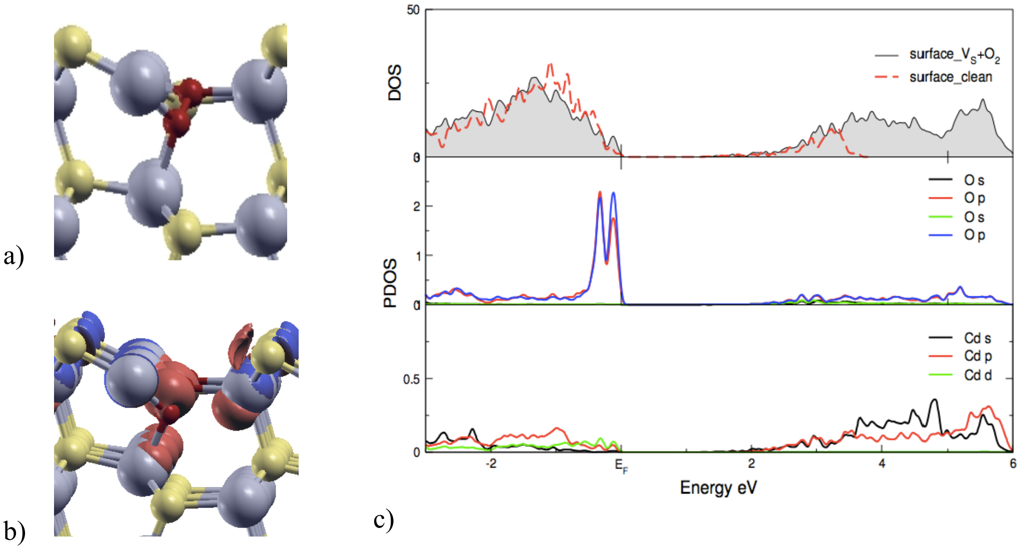

Figure 5.9: Left: side view of relaxed interaction between defective surfaceV$_{S-hollow}$ and O_2(a) bondin-charge of interaction (b) Right: Calculated total DOS and projected DOS of of defective surface and oxygen (c).

$\underline{H_2O\ @\ V_S^{hollow}}$ - In the case of H_2O on top of V_S^{hollow}, the molecule resulted adsorbed on the Cd$_{NN}$ forming a bond of 2.39Å (see Fig. 5.10-a).

In figure 5.10-b a re-arrangement of the charge resulted in an accumulation in the region between H_2O and S in top position and partially between oxygen and Cd. The adsorption energy of this system was E$_{ad}$ = -66.84 kJmol^{-1}, lower than that found in the adsorption of O_2 on the same defect. The CdS valence band is modified, in the region close to the Fermi energy, by the O-p orbital, as shown in figure 5.10-c).

In order to better understand the behavior of CdS with water molecules, two isolated atoms of Cd and S were embedded in a cluster of 32 H_2O (see Fig. 5.11, right side). The relaxed system showed the formed CdS (the bond distance is again of 2.38Å) surrounded by a network of hydrogen-bonded water molecules. Two of them are linked to the Cd ion, assuming a trigonal planar geometry, with one bond of 2.36Å and one of 2.18Å. The two angles $H\hat{O}H$ of H_2O increased from the typical experimental value

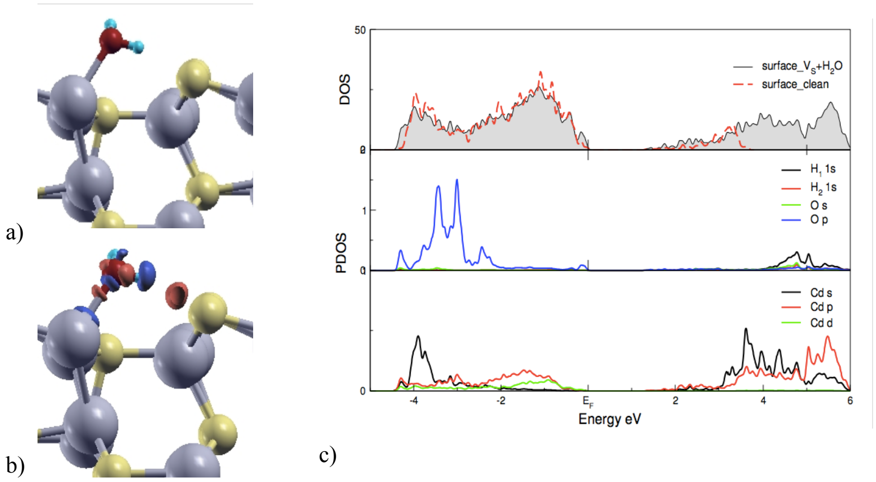

Figure 5.10: Left: side view of relaxed interaction between defective surface V_S^{hollow} and H_2O(a) bondin-charge of interaction (b) Right: Calculated total DOS and projected DOS of of defective surface and oxygen (c).

of 104.50° to 108.27° and 108.05°, respectively. The geometry of Cd ion and the two water bonded molecules is very similar, in terms of distances and orientations, to that found in studies on divalent cadmium solvation shell [136]. Conversely, sulfur atom does not directly participate to the bonds with oxygen.

In summary, the defective surface appeared more reactive than clean surface, as expected. The presence of oxygen and water molecules in defective surface resulted in considerable changes both in the geomety (see 5.5-a, 5.9-a) and in the electronic structure (see 5.5, see 5.7-c) where trap states, differently located, are present in the gap depending on the kind of vacancy site. Calculations on bigger supercells, where a larger number of molecules interact with the surface are in progress.

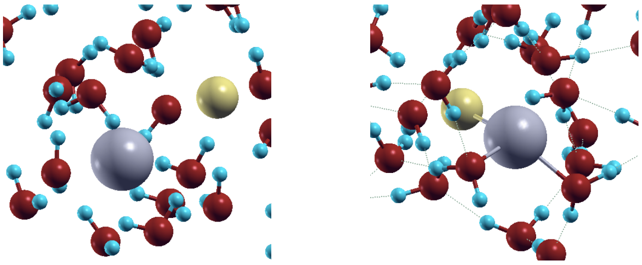

Figure 5.11: Interaction between the CdS and H_2O molecules: initial configuration (left) and final configuration (right)

CONCLUSIONS

Structural defects in CdS - compound widely used as yellow pigment by prominent 19th to 20th century artists such as Claude Monet, Vincent Van Gogh, Pablo Picasso and Henry Matisse - may play a role in the degradation process at the surface of impressionist paintings.

In this thesis a thourogh study on native point defects, namely Cd and S vacancies in both wurtzite bulk and $[10\bar{1}0]$ surface were investigated within the framework of first principles calculations based on DFT-GGA. Geometry, electronic structure and energetics for all possible kinds of non equivalent vacancies within the volume and the surface were studied. The results from the calculations can be summarized in the following points:

Bulk - *i)* Cd and S vacancies (V_{Cd} and V_S) in bulk wurtzite induce a inward relaxation with a more relevant effect in V_S where Cd atoms nearest neighboring the vacancy site originates three new Cd-Cd bonds cadmium. This is likely a strong Jahn-Teller distortion that became visible only in the larger simulation cell. It requires further investigation on the orbital occupations that is still in progress. V_{Cd}, conversely shows in the density of states a spin contribution crossing the Fermi energy due to S_{NN} 3*p*-states (dangling bonds). These results find analogies in CdS zincblende where a magnetization effect appears in the Cd vacancy and not in S vacancy.

$[10\bar{1}0]$ surface - Two non-equivalent positions for vacancy sites were studied both for Cd and S, namely *top* and *hollow* vacancies. The calculations were performed in a 2x1 surface and in a larger one, 2x2, to reduce possible size effects.

As for the Cd vacancy, the overall geometry, in both V_{Cd}^{top} and V_{Cd}^{hollow}, shows an inward relaxation of NN atoms with the participation of cadmium atoms from the layer below that raise toward the vacancy. Remarkably, both V_{Cd}^{top} and V_{Cd}^{hollow} induce an acceptor level in the band gap. It originates from the spin-down contribution coming from $3p$-orbitals of S_{NN}. Attributing the correct value to a Kohn-Sham eigenvalue within a band gap, requires extensive calculations beyond the standard ground state approach used in the present work, due to the discontinuity in the exchange and correlation functional. Difficult but not impossible, optical absorptions are needed to be studied in the follow-up of this work. Nevertheless, an empirical approximation allowed us to evaluate the position of these peaks. More specifically, GW calculations on bulk CdS were performed to obtain the correct energy gap for cadmium sulfide that combined with E_{VBM} and the band gap center led to a correct estimate of the gap in the system containing the defective surface. Empirically rescaling the Kohn-Sham peak to the correct gap we obtained for V_{Cd}^{top} a value corresponding to an emission band of 1.26 eV (984 nm) and for V_{Cd}^{hollow} two emission bands of 1.43 eV (867 nm) and 1.54 eV (805 nm). These values fall in the range, near infrared-red, of spectroscopic measurements performed by means of luminescence techniques on degraded yellow pigments and predicts that Cd vacancies are the best candidates to be the most reactive sites in the interaction between the surface and, as we will see later, the external agents.

Since historical information on the growth conditions of the pigments is often lacking, the formation energies for all the defects were calculated in two extreme growth conditions, namely S-rich and Cd-rich. The formation energy of V_{Cd}^{hollow} and V_{Cd}^{top} are the lowest among the four possible surface vacancies in S-rich growth condition. In Cd-rich, the defect formation energy turns out to be lower for V_S^{top} and V_S^{hollow}. Interestingly, a thorough understanding of the features of such defects and their influence on the behavior of the CdS surface, can add information on the history of the sample as well as the environment during the synthesis.

Sulfur vacancies, show an inward relaxation and no extra levels within the band gap, expect for a rearrangement of electron state in the CBM region in V_S^{top}.

O_2 and H_2O @ [$10\bar{1}0$] surface - To preliminary simulate the interaction between the CdS surface and external agents some simplified models were considered. More specifically, one molecule of oxygen, water and a combination of them was placed on top of the clean and the defective surface. The clean surface appears unreactive: the molecules are physisorbed and no charge transfer was observed in all the mentioned systems. The behavior of the defective surface was different, as expected. Separately, O_2 and H_2O were considered on top of the defects that, depending on the band structure, turned out to be the most reactive: V_{Cd}^{top} and V_S^{hollow}. As for the molecules on V_{Cd}^{top} we found that the acceptor level representing a hole in the sulfur site persists in the presence of oxygen whose p-states hybridize with S dangling bonds. The estimate of this peak was associated to an emission band of 1.12 eV (1107 nm - near infrared).

The oxygen molecule resulted chemisorbed to S_{NN} nearby the vacancy. The sulfur-surface distance is elongated and the sulfur bond to O_2 is emerging from the surface. From the local charge analysis, it results an accumulation of charge on O_2 and a loss of charge on S. The hypothesis of reaction invoked by experiments, $CdS + 2O_2 \longrightarrow Cd^{2+} + SO^{4-}$, in a photo-oxydation mechanism leading to the pigment degradation, make us confident on the fact that the formation of SO_2 obtained in the calculations is likely to be a part of the overall reaction path. A more realistic model (higher coverage and larger supercell) is required to shed light on this very interesting point. The presence of H_2O, as opposite to O_2, does not lead to extra peaks in the band gap. A recombination electron-hole is likely to happen as a consequence of the adsorption. The molecule is chemisorbed on top of S_{NN}. In this case a transfer of charge from the surface to the water molecule is observed. The study of a combination of the two molecules on the defective surface is still in progress.

The O_2 molecule on V_S^{hollow} has a relevant behavior from a geometrical point of view. It results fully embedded in the CdS surface and occupies a substitutional position replacing a S atom. The two oxygen atoms are bond to Cd_{NN}. No extra peaks appear in the band gap. The water molecule is chemisorbed on Cd_{NN} where a charge transfer from the surface, mostly from Cd, in favor of oxygen is calculated. Notice, whilst water molecules tend to form Cd-O bonds, O_2 can bind both with S and Cd.

In few words, the Cd vacancy appears to have a key role in the reactivity of the CdS surface and the presence of this defects is the likely to be the driving force for the more complex photo-oxydation reactions invoked by experiments. This is due to the extra acceptor level, originating from S dangling bonds, predicted in the near-infrared region that turns out to be in excellent agreement with luminescence measurements on CdS pigments both commercial and historical.

At this point a more accurate determination of the location of extra peaks in the band gap, by means of time-dependent DFT of fully GW methods, is strongly required to attribute the correct value to the trap levels. Considering the possibility to investigate in a broader spectral range, such theoretical method would be helpful in the interpretation of experimental evidences obtained via luminescence analysis.

Bibliography

[1] C. Freysoldt, B. Grabowski, T. Hickel, J. Neugebauer, G. Kresse, A. Janotti, and C. G. Van de Walle. First-principles calculations for point defects in solids. *Rev. Mod. Phys.*, 86:253–305, Mar 2014.

[2] N. Kazume, S. Takuya, Y. Matsukura, M. Baba, M. Hasegawa, and T. Sasaki. Density-functional electronic structure calculations for native defects and Cu impurities in CdS. *Phys. Rev. B*, 74:035210, Jul 2006.

[3] A. S. Barnard, , and H. Xu. First Principles and Thermodynamic Modeling of CdS Surfaces and Nanorods. *The Journal of Physical Chemistry C*, 111(49):18112–18117, 2007.

[4] A Romeo, D.L Bätzner, H Zogg, C Vignali, and A.N Tiwari. Influence of CdS growth process on structural and photovoltaic properties of CdTe/CdS solar cells. *Solar Energy Materials and Solar Cells*, 67(1–4):311 – 321, 2001. {PVSEC} 11 - {PART} {III}.

[5] A. L. Fahrenbruch and R. H. Bube. *Fundamentals of solar cells: photovoltaic solar energy conversion.* New York: Academic Press, 1983.

[6] K. L. Chopra and S. R. Das. *Why Thin Film Solar Cells*, pages 1–18. Springer US, 1983.

[7] A. A. Morales. Can we improve the record efficiency of CdS/CdTe solar cells. *Solar Energy Materials and Solar Cells*, 90(15):2213 – 2220, 2006. Selected Papers from the Solar Cells and Solar Energy Materials Symposium -IMRC 2005XIV International Materials Research Congress.

[8] T.D. Dzhafarov, M. Altunbas, A. I. Kopya, V. Novruzov, and E. Bacaksiz. Formation of p-type CdS thin films by laser-stimulated copper diffusion. *Journal of Physics D: Applied Physics*, 32(24):L125, 1999.

[9] X. Duan, Y. Huang, R. Agarwal, and C.M. Lieber. Single-nanowire electrically driven lasers. *Nature*, 421:241–245, 2003.

[10] N. V. Hullavarad, S. S. Hullavarad, and P. C. Karulkar. Cadmium Sulphide (CdS) nanotechnology: Synthesis and Applications. *Journal of Nanoscience and Nanotechnology*, 8(7):3272–3299(28), 2008.

[11] A. Merkoçi, L. Humberto Marcolino-Junior, S. Marín, O. Fatibello-Filho, and S. Alegret. Detection of cadmium sulphide nanoparticles by using screen-printed electrodes and a handheld device. *Nanotechnology*, 18(3):035502, 2007.

[12] E. Deligoz, K. Colakoglu, and Y. Ciftci. Elastic, electronic, and lattice dynamical properties of CdS, CdSe, and CdTe. *Physica B: Condensed Matter*, 373(1):124 – 130, 2006.

[13] A.R. Jiavani and A.R. Jani. Elastic properties of group IV semiconductors by pseudopotential approach. *International Journal of moderm physics B.*, 25(27):3569–3582, 2011.

[14] A.R. Jivani, H.J. Trivedi, P.N. Gajjar, and A.R. Jani. Condensed Matter: Electronic Structure, Electrical, Magnetic and Optical Properties - Electronic properties of Cds, CdSe and CdTe semiconductor binary alloys. *in: Indian journal of pure and applied physics (New Delhi : Inst), Vol. 44, No. 1 (2006), p. 59-61 Indian Journal of pure and applied physics*, 44(1):59–61, 2006.

[15] W. G. Huckle, G. F. Swigert, and S. E. Wiberley. Cadmium pigments. structure and composition. *I&EC Product Research and Development*, 5(4):362–366, 1966.

[16] J. Paulus and U. Knuutinen. Cadmium colours: composition and properties. *Applied Physics A*, 79(2):397–400, 2004.

[17] G. Van der Snickt, K. Janssens, J. Dik, F. De Nolf, W.and Vanmeert, J. Jaroszewicz, M. Cotte, G. Falkenberg, and L. Van der Loeff. Combined use of Synchrotron Radiation Based Micro-X-ray Fluorescence, Micro-X-ray Diffraction, Micro-X-ray Absorption Near-Edge, and Micro-Fourier Transform Infrared Spectroscopies for Revealing an Alternative Degradation Pathway of the Pigment Cadmium Yellow in a Painting by Van Gogh. *Analytical Chemistry*, 84(23):10221–10228, 2012. PMID: 22931047.

[18] I. Fiedler and M. Bayard. *Artists' Pigments, A Handbook of Their History and Characteristics*, volume 1. National Gallery of Art/Cambridge University, 1986.

[19] E. Eastaugh, V. Walsh, T. Chaplin, and R. Siddall. *Pigment Compendium: A Dictionary of Historical Pigments.* 2007.

[20] A. P. Davis and C.P. Huang. The photocatalytic oxidation of sulfur-containing organic compounds using cadmium sulfide and the effect on CdS photocorrosion. *Water Research*, 25(10):1273 – 1278, 1991.

[21] R. Williams. *J. Chem. Phys.*, (32):1505–1514, 1960.

[22] G. Van der Snickt, J. Dik, M. Cotte, K. Janssens, J. Jaroszewicz, W. De Nolf, J. Groenewegen, and L. Van der Loeff. Characterization of a Degraded Cadmium Yellow (CdS) Pigment in an Oil Painting by Means of Synchrotron Radiation based X-ray Techniques. *Analytical Chemistry*, 81(7):2600–2610, 2009. PMID: 19278249.

[23] J. Mass, J. Sedlmair, C. S. Patterson, David Carson, B. Buckley, and C. Hirschmugl. SR-FTIR imaging of the altered cadmium sulfide yellow paints in Henri Matisse's Le Bonheur de vivre (1905-6) - examination of visually distinct degradation regions. *Analyst*, 138:6032–6043, 2013.

[24] J. L. Mass, R. Opila, B. Buckley, M. Cotte, J. Church, and A. Mehta. The photodegradation of cadmium yellow paints in Henri Matisse's Le Bonheur de vivre (1905–1906). *Applied Physics A*, 111(1):59–68, 2013.

[25] A. H. Church. *The Chemistry of Paints and Painting.* Seeley and Co, London, 1 st edn edition, 1890.

[26] E. Pouyet, M. Cotte, B. Fayard, M. Salomé, F. Meirer, A. Mehta, E.S. Uffelman, A. Hull, F. Vanmeert, J. Kieffer, M. Burghammer, K. Janssens, F. Sette, and J. Mass. 2D X-ray and FTIR micro-analysis of the degradation of cadmium yellow pigment in paintings of Henri Matisse. *Applied Physics A*, pages 1–14, 2015.

[27] B. Leone and al. The deterioration of cadmium sulphide yellow artists' pigments. In James & James, editor, *Triennial meeting (14th), The Hague, 12–16 September 2005*, 2005.

[28] B. Topalova-Casadiego and Plahter U. The National Gallery Technical Bulletin 30th Anniversary Conference. pages 244–252, 2011.

[29] T. Miyoshi, M. Ikeya, S. Kinoshita, and T. Kushida. Laser-Induced Fluorescence of Oil Colours and its Application to the Identification of Pigments in Oil Paintings. *Japanese Journal of Applied Physics*, 21(7R):1032, 1982.

[30] I. Borgia, R. Fantoni, C. Flamini, T. Di Palma, A. Giardini Guidoni, and A. Mele. Luminescence from pigments and resins for oil paintings induced by laser excitation. *Applied Surface Science*, 127–129(0):95 – 100, 1998.

[31] T. Miyoshi. Fluorescence from Varnishes for Oil Paintings under N_2 Laser Excitation. *Japanese Journal of Applied Physics*, 26(5R):780, 1987.

[32] H. Haken and Nikitine S. *Excitons at High Density*, volume 73. Springer Berlin Heidelberg and New York, 1975.

[33] Rao C. N. R. *Ultraviolet and Visible Spectroscopy*, volume 1. Butter-worth, London, 1967.

[34] S. Shionoya and W. H. Hen. *Phosphor Handbook*. CRC Press, Boca Raton, FL, 1997.

[35] D. F. Barnes. *Infrared luminescence of minerals*. Number 71 in 1052 C. Geol. Survey Bull., 1958.

[36] C. F. Bridgman and Gibson H. Lou. Infrared luminescence in the photographic examination of paintings and other art objects. *Studies in Conservation*, 8(3):77–83, 1963.

[37] V. Babentsov and F. Sizov. Defects in quantum dots of IIB–VI semiconductors. *Opto-Electronics Review*, 16(3):208–225, 2008.

[38] A. Cesaratto, C. D'Andrea, A. Nevin, G. Valentini, F. Tassone, R. Alberti, T. Frizzi, and D. Comelli. Analysis of cadmium-based pigments with time-resolved photoluminescence. *Anal. Methods*, 6:130–138, 2014.

[39] M. Thoury, J. K. Delaney, René de la Rie E., M. Palmer, K. Morales, and Krueger J. Near-Infrared Luminescence of Cadmium Pigments: In Situ Identification and Mapping in Paintings. *Appl. Spectrosc.*, 65(8):939–951, Aug 2011.

[40] A. Nevin, A. Cesaratto, S. Bellei, C. D'Andrea, L. Toniolo, G. Valentini, and D. Comelli. Time-Resolved Photoluminescence Spectroscopy and Imaging: New Approaches to the Analysis of Cultural Heritage and Its Degradation. *Sensors*, 14(4):6338, 2014.

[41] D. Comelli, A. Nevin, A. Brambilla, I. Osticioli, G. Valentini, L. Toniolo, M. Fratelli, and R. Cubeddu. On the discovery of an unusual luminescent pigment in Van Gogh's painting "Les bretonnes et le pardon de pont Aven". *Applied Physics A*, 106(1):25–34, 2012.

[42] A. Varghese, P. Ghosh, and S. Datta. Cadmium vacancy minority defects as luminescence centers in size and strain dependent photoluminescence shifts in CdS Nanotubes. *The Journal of Physical Chemistry C*, 118(37):21604–21613, 2014.

[43] C. Hogan and F. Da Pieve. Colour degradation of artworks: an ab initio approach to X-ray, electronic and optical spectroscopy analyses of vermilion photodarkening. *J. Anal. At. Spectrom.*, 30:588–598, 2015.

[44] F. Da Pieve, C. Hogan, D. Lamoen, J. Verbeeck, F. Vanmeert, M. Radepont, M. Cotte, K. Janssens, X. Gonze, and G. Van Tendeloo. Casting Light on the Darkening of Colors in Historical Paintings. *Phys. Rev. Lett.*, 111:208302, Nov 2013.

[45] P. Yu and M. Cardona. *Fundamentals of Semiconductors: Physics and Materials Properties*. Graduate Texts in Physics. Springer Berlin Heidelberg, 2010.

[46] L. Giacopetti and A. Satta. Degradation of Cd-yellow paints: Ab initio study of native defects in {10.0} surface CdS. *Microchemical Journal*, pages –, 2015.

[47] M. Born and J.R. Oppenheimer. *Ann. Phys.*, 84(457), 1927.

[48] S. Biswajit. *Density-Functional Theory Exchange-Correlation Functionals for Hydrogen Bonds in Water*. PhD thesis, Von der Fakultät II Mathematik und Naturwissenschaften der Technischen Universität Berlin, 2010.

[49] S. O. Odoh, C. J. Cramer, D. G. Truhlar, and L Gagliardi. Quantum-Chemical Characterization of the Properties and Reactivities of Metal–Organic Frameworks. *Chemical Reviews*, 115(12):6051–6111, 2015. PMID: 25872949.

[50] P. Hohenberg and W. Kohn. Inhomogeneous electron gas. *Phys. Rev.*, 136:B864–B871, Nov 1964.

[51] R.M. Dreialer and E.K.U. Gross. *Density Functional Theory: An Approach to Quantum Many Body Problem*. Springer-Verlag, Berlin, 1990.

[52] W. Kohn. Density Functional Theory: Fundumentals and Application. In Fumi F. Tosi M.P. Bassani F., editor, *Highlight of Condensed Matter Theory*, pages 1–15, 1985.

[53] K. I. Ramachandran, G Deepa, and K. Namboori. *Computational Chemistry and Molecular Modeling: Principles and Applications: Principles and Applications.* Springer Science & Business Media, 2008.

[54] J. Labanowski. *Simplified and Biased Introduction to Density Functional Approaches in Chemistry.* Ohio Supercomputer Center, Ohio Supercomputer Center, 1224 Kinnear Rd, Columbus, OH 43221-1153.

[55] W. Kohn and L. J. Sham. Self-Consistent Equations Including Exchange and Correlation Effects. *Phys. Rev.*, 140:A1133–A1138, Nov 1965.

[56] P. D. Haynes. *Linear-scaling methods in ab initio quantum-mechanical calculations.* PhD thesis, Christ's College, Cambridge, 1998.

[57] D. M. Ceperley and B. J. Alder. Ground State of the Electron Gas by a Stochastic Method. *Phys. Rev. Lett.*, 45:566–569, Aug 1980.

[58] J. P. Perdew and A. Zunger. Self-interaction correction to density-functional approximations for many-electron systems. *Phys. Rev. B*, 23:5048–5079, May 1981.

[59] J. P. Perdew and Y. Wang. Accurate and simple analytic representation of the electron-gas correlation energy. *Phys. Rev. B*, 45:13244–13249, Jun 1992.

[60] S. H. Vosko, L. Wilk, and M. Nusair. Accurate spin-dependent electron liquid correlation energies for local spin density calculations: a critical analysis. *Canadian Journal of Physics*, 58(8):1200–1211, 1980.

[61] C. J. Cramer. *Essentials of Computational Chemistry.* Wiley: Chichester, 2002.

[62] V. N. Staroverov, G. E. Scuseria, J. Tao, and J. P. Perdew. Tests of a ladder of density functionals for bulk solids and surfaces. *Phys. Rev. B*, 69:075102, Feb 2004.

[63] J. Harl, L. Schimka, and G. Kresse. Assessing the quality of the random phase approximation for lattice constants and atomization energies of solids. *Phys. Rev. B*, 81:115126, Mar 2010.

[64] K. Capelle. A Bird's-eye view of Density-Functional Theory. *Brazilian Journal of Physics*, 36:1318 – 1343, 12 2006.

[65] J. P. Perdew, A. Ruzsinszky, J. Tao, V. N. Staroverov, G. E. Scuseria, and G. I. Csonka. Prescription for the design and selection of density functional approximations: More constraint satisfaction with fewer fits. *The Journal of Chemical Physics*, 123(6), 2005.

[66] J. P. Perdew, K. Burke, and M. Ernzerhof. Generalized Gradient Approximation made simple. *Phys. Rev. Lett.*, 77:3865–3868, Oct 1996.

[67] O. Ziesche and H. Eschrig. *Electronic structure of solids '91: proceedings of the 75. WE-Heraeus-Seminar and 21st Annual International Symposium on Electronic Structure of Solids held in Gaussig (Germany), March 11-15, 1991*, volume 17 of *Physical research*. Akademie Verlag, 1991.

[68] L. Chengteh, W. Yang, and R. G. Parr. Development of the Colle-Salvetti correlation-energy formula into a functional of the electron density. *Phys. Rev. B*, 37:785–789, Jan 1988.

[69] J. P. Perdew. Density-functional approximation for the correlation energy of the inhomogeneous electron gas. *Phys. Rev. B*, 33:8822–8824, Jun 1986.

[70] C. Kittel. *Introduction to Solid State Physics*. John Wiley & Sons, New York, seventh ed. edition, 1996.

[71] E. Kaxiras. *Atomic and Electronic Structure of Solids*. Cambridge University Press, 2003.

[72] H. J. Monkhorst and J. D. Pack. Special points for Brillouin-zone integrations. *Phys. Rev. B*, 13:5188–5192, Jun 1976.

[73] M. C. Payne, M. P. Teter, D. C. Allan, T. A. Arias, and J. D. Joannopoulos. Iterative minimization techniques for *ab initio* total-energy calculations: molecular dynamics and conjugate gradients. *Rev. Mod. Phys.*, 64:1045–1097, Oct 1992.

[74] X. Hu. *First Principles Studies of Water and Ice on Oxide Surfaces*. PhD thesis, University College London, Department of Chemistry, January 2010.

[75] S. Clark. *Complex Structures In Tetrahedrally Bonded Semiconductor*. PhD thesis, University of Edinburgh, 1994.

[76] P. Giannozzi. *Numerical Methods in Quantum Mechanics*. University of Udine, 2015.

[77] D. R. Hamann. Generalized norm-conserving pseudopotentials. *Phys. Rev. B*, 40:2980–2987, Aug 1989.

[78] D. R. Hamann, M. Schlüter, and C. Chiang. Norm-conserving pseudopotentials. *Phys. Rev. Lett.*, 43:1494–1497, Nov 1979.

[79] N. M. Neshev and E. I. Proinov. Xα sw estimation of the degree of localization of 3d and 2p states in transition metal oxides. *Journal of Molecular Catalysis*, 54(3):484 – 489, 1989.

[80] N. Troullier and J. Martins. Efficient pseudopotentials for plane-wave calculations. *Phys. Rev. B*, 43:1993–2006, Jan 1991.

[81] S. Goedecker, M. Teter, and J. Hutter. Separable dual-space Gaussian pseudopotentials. *Phys. Rev. B*, 54:1703–1710, Jul 1996.

[82] D. Vanderbilt. Soft self-consistent pseudopotentials in a generalized eigenvalue formalism. *Phys. Rev. B*, 41:7892–7895, Apr 1990.

[83] G. Kresse and D. Joubert. From ultrasoft pseudopotentials to the projector augmented-wave method. *Phys. Rev. B*, 59:1758–1775, Jan 1999.

[84] S. J. Clark, C. J. Segall, M. D. andPickard, P. J. Hasnip, M. J. Probert, K. Refson, and M. C. Payne. First principles methods using CASTEP. *Zeitschrift fuer Kristallographie*, 220:567–570, 2005.

[85] R. Guerra. *Silicon Nanocrystals: Fundamental Theory and First-Principle Calculations*. PhD thesis, University of Modena.

[86] G. Kresse and J. Hafner. Norm-conserving and ultrasoft pseudopotentials for first-row and transition elements. *Journal of Physics: Condensed Matter*, 6(40):8245, 1994.

[87] C. Friedrich and A. Schindlmayr. *Many-Body Perturbation Theory: The GW Approximation*, volume 31 of *NIC Series*. Computational Nanoscience: Do It Yourself! - Lecture Notes, 2006.

[88] H. Jiang. Electronic band structure from first-principles Green's function approach: theory and implementations. *Frontiers of Chemistry in China*, 6(4):253–268, 2012.

[89] F. Aryasetiawan and O. Gunnarsson. The gw method. *Reports on Progress in Physics*, 61(3):237, 1998.

[90] J. Harl. *The linear response function in density functional theory.* PhD thesis, Universität Wien, 2008.

[91] P. Umari, G. Stenuit, and S. Baroni. Optimal representation of the polarization propagator for large-scale *GW* calculations. *Phys. Rev. B*, 79:201104, May 2009.

[92] P. Umari, G. Stenuit, and S. Baroni. GW quasiparticle spectra from occupied states only. *Phys. Rev. B*, 81:115104, Mar 2010.

[93] B. Walker, A. M. Saitta, R. Gebauer, and S. Baroni. Efficient Approach to Time-Dependent Density-Functional Perturbation Theory for Optical Spectroscopy. *Phys. Rev. Lett.*, 96:113001, Mar 2006.

[94] D. Rocca, R. Gebauer, Y. Saad, and S. Baroni. Turbo charging Time-Dependent Density-Functional theory with Lanczos chains. *The Journal of Chemical Physics*, 128(15), 2008.

[95] L. Hedin. New Method for Calculating the One-Particle Green's Function with Application to the Electron-Gas Problem. *Phys. Rev.*, 139:A796–A823, Aug 1965.

[96] M. S. Hybertsen and S. G. Louie. Electron correlation in semiconductors and insulators: Band gaps and quasiparticle energies. *Phys. Rev. B*, 34:5390–5413, Oct 1986.

[97] Y. Saad. *Iterative Methods for Sparse Linear Systems.* SIAM, Philadelphia, 2 edition, 2003.

[98] J. Heyd, J. E. Peralta, G. E. Scuseria, and R. L. Martin. Energy band gaps and lattice parameters evaluated with the heyd-scuseria-ernzerhof screened hybrid functional. *The Journal of Chemical Physics*, 123(17):–, 2005.

[99] F. Tran and P. Blaha. Accurate Band Gaps of Semiconductors and insulators with a Semilocal Exchange-Correlation Potential. *Phys. Rev. Lett.*, 102:226401, Jun 2009.

[100] W. G. Aulbur, M. Städele, and A. Görling. Exact-exchange-based quasiparticle calculations. *Phys. Rev. B*, 62:7121–7132, Sep 2000.

[101] M. Shishkin, M. Marsman, and G. Kresse. Accurate Quasiparticle Spectra from Self-Consistent GW Calculations with Vertex Corrections. *Phys. Rev. Lett.*, 99:246403, Dec 2007.

[102] P. Jakubas. *Theory of generation of Frenkel pairs in semiconductors: consequences for electric, magnetic, and structural properties.* PhD thesis, Institute of Physics, Polish Academy of Sciences, June 2009.

[103] I. Khan, I. Ahmad, H. A. R. Aliabad, and M. Maqbool. Accurate theoretical bandgap calculations of II-VI semiconductors. *eprint arXiv:1201.0870*, 2012.

[104] M. C. Toroker, D. K. Kanan, N. Alidoust, L. Y. Isseroff, P. Liao, and E. A. Carter. First principles scheme to evaluate band edge positions in potential transition metal oxide photocatalysts and photoelectrodes. *Phys. Chem. Chem. Phys.*, 13:16644–16654, 2011.

[105] M. C. Payne, M. P. Teter, D. C. Allan, T. A. Arias, and J. D. Joannopoulos. Iterative minimization techniques for *ab initio* total-energy calculations: molecular dynamics and conjugate gradients. *Rev. Mod. Phys.*, 64:1045–1097, Oct 1992.

[106] W. Liu, W. T. Zheng, and Q. Jiang. First-principles study of the surface energy and work function of III-V semiconductor compounds. *Phys. Rev. B*, 75:235322, Jun 2007.

[107] M. J. Rutter and J. Robertson. *Ab initio* calculation of electron affinities of diamond surfaces. *Phys. Rev. B*, 57:9241–9245, Apr 1998.

[108] G. Onida, L. Reining, and A. Rubio. Electronic excitations: density-functional versus many-body Green's-function approaches. *Rev. Mod. Phys.*, 74:601–659, Jun 2002.

[109] J. P. Perdew and M. Levy. Physical content of the exact Kohn-Sham orbital energies: Band gaps and derivative discontinuities. *Phys. Rev. Lett.*, 51:1884–1887, Nov 1983.

[110] J. F. Janak. Proof that $\frac{\partial e}{\partial n_i} = \epsilon$ in density-functional theory. *Phys. Rev. B*, 18:7165–7168, Dec 1978.

[111] W. G. Aulbur, J. Lars, and J. W. Wilkins. *Quasiparticle Calculations in Solids*, volume 54 of *Solid State Physics.* Academic Press, 1999.

[112] J. W. Jr. Morris. *A Survey of materials Science.* PhD thesis, Department of Materials Science and Engineering, University of California, Berkeley, 2008.

[113] A. Prabhakar. *Investigations of deep level defects in semiconductor material systems.* PhD thesis, California Istitute of Technology, 1985.

[114] M. J. Spaeth and H. Overhof. *Point Defects in Semiconductors and Insulators: Determination of Atomic and Insulators: Determination of Atomic and Electronic Structure from Paramagnetic Hyperfine.* Springer Science & Business Medi, 2013.

[115] J. S. Steckel, J. P. Zimmer, S. Coe-Sullivan, N. E. Stott, V. Bulović, and M. G. Bawendi. Blue Luminescence from (Cds)ZnS core–shell nanocrystals. *Angewandte Chemie International Edition*, 43(16):2154–2158, 2004.

[116] P. Giannozzi and al. QUANTUM ESPRESSO: a modular and open-source software project for quantum simulations of materials. *Journal of Physics: Condensed Matter*, 21(39):395502, 2009.

[117] C. Hartwigsen, S. Goedecker, and J. Hutter. Relativistic separable dual-space Gaussian pseudopotentials from H to Rn. *Phys. Rev. B*, 58:3641–3662, Aug 1998.

[118] E. S. Rittner and J. H. Schulman. Studies on the Coprecipitation of Cadmium and Mercuric Sulfides. *The Journal of Physical Chemistry*, 47(8):537–543, 1943.

[119] F.D. Murnaghan. *Proc. Natl. Acad. Sci. U.S.A.*, (30):5390, 1944.

[120] S. Biering and P. Schwerdtfeger. A comparative density functional study of the high-pressure phases of solid ZnX, CdX, and HgX (X = S, Se, and Te): Trends and relativistic effects. *The Journal of Chemical Physics*, 137(3), 2012.

[121] N.A. Razik. Use of a standard reference material for precise lattice parameter determination of materials of hexagonal crystal structure. *Journal of Materials Science Letters*, 6(12):1443–1444, 1987.

[122] U. Pal, R. Silva-González, G. Martínez-Montes, M. Gracia-Jiménez, M. A. Vidal, and S. Torres. Optical characterization of vacuum evaporated cadmium sulfide films. *Thin Solid Films*, 305(1–2):345 – 350, 1997.

[123] JP. Tang, L. Wang, HJ. Luo, and WZ. Xiao. Magnetic properties in zinc-blende CdS induced by Cd vacancies. *Physics Letters A*, 377(7):572 – 576, 2013.

[124] A. Zitouni, S. Bentata, W. Benstaali, and B. Abbar. Ab-initio study of structural, electronic and magnetic properties of CdTe doped transition metal Co. *Solid State Communications*, 190:40 – 43, 2014.

[125] K. P. Tchakpele, J. P. Albert, and C. Gout. Study of ideal vacancies in CdS (wurtzite). *Phys. Rev. B*, 27:1244–1250, Jan 1983.

[126] A. Kobayashi, O. F. Sankey, and J. D. Dow. Deep energy levels of defects in the wurtzite semiconductors AIN, CdS, CdSe, ZnS, and ZnO. *Phys. Rev. B*, 28:946–956, Jul 1983.

[127] A. Casini, F. Lotti, M. Picollo, L. Stefani, and A. Aldrovandi. Fourier Transform Interferometric Imaging Spectrometry: A New Tool for the Study of Reflectance and Fluorescence of Polychrome Surfaces. In J. H. Townsend, K. Eremin, and A. Adriaens, editors, *Conservation Science 2002*, 2003.

[128] R. Rosi, C. Grazia, F. Gabrieli, A. Romani, M. Paolantoni, R. Vivani, B. G. Brunetti, P. Colomban, and C. Miliani. UV–Vis-NIR and micro Raman spectroscopies for the non destructive identification of $Cd_{1-x}Zn_xS$ solid solutions in cadmium yellow pigments. *Microchemical Journal*, 124:856 – 867, 2016.

[129] W. Liu, C. Jia, C. Jin, L. Yao, W. Cai, and X. Li. Growth mechanism and photoluminescence of CdS nanobelts on Si substrate. *Journal of Crystal Growth*, 269(2–4):304 – 309, 2004.

[130] J. Chrysochoos. Recombination luminescence quenching of nonstoichiometric cadmium sulfide clusters by ZnTPP. *The Journal of Physical Chemistry*, 96(7):2868–2873, 1992.

[131] J. J. Ramsden and M. Gratzel. Photoluminescence of small cadmium sulphide particles. *J. Chem. Soc., Faraday Trans. 1*, 80:919–933, 1984.

[132] S. Grimme. Semiempirical GGA-Type Density Functional Constructed with a Long-Range Dispersion Correction. *J. Comput. Chem.*, 27(15):1787–1799, 2006.

[133] V. Barone, M. Casarin, D. Forrer, M. Pavone, M. Sambi, and A. Vittadini. Role and effective treatment of dispersive forces in materials: Polyethylene and graphite crystals as test cases. *Journal of Computational Chemistry*, 30(6):934–939, 2009.

[134] D. Eisenberg and W. Kauzmann. *The Structure and properties of water*. Oxford Classic Texts in the Physical Sciences, 2005.

[135] G. Henkelman and H. Jónsson. Improved Tangent Estimate in the Nudged Elastic Band Method for Finding Minimum Energy Paths and Saddle Points. *J. Phys. Chem.*, 113:9978–99715, 2000.

[136] C. Kritayakornupong, K. Plankensteiner, and B. M. Rode. Structure and Dynamics of the Cd^{2+} Ion in Aqueous Solutio: Ab initio QM/MM Molecular Dynamics Simulationolution: ab initio qm/mm Molecular Dynamics Simulation. *The Journal of Physical Chemistry A*, 107(48):10330–10334, 2003.

Acknowledgments

I am very grateful to Alessandra Satta, my supervisor who has giving me a big support not only in the work matters but also in my life struggling. In particular a special thanks for her guidance and constant help in the project development. Her constant positive outlook has always helped me to make all less difficult. Without her help this thesis would not be the same as this final redation. These three and a half years of working with her has been a great learning and mixed with fun too. On top of this, my very special thanks go to Giovanna Masala, Paolo Ruggerone, Danilo Addari and my colleges in particular Barbara Maccioni who has listened to my problems and helped me to get closer to the solutions. Finally, I am grateful for all the encouragement from my family and my friends. The authors acknowledge RAS (Regione autonoma della Sardegna) and Fondazione Banco di Sardegna for partial financial support. This work was carried out using the HPC infrastructures of CRS4, Pula (Ca), Italy. L. G. and A. S. are greatly indebted to Dr. Jennifer Mass for fruitful discussions.